Design, manufacturing and performance OF Fe–Mn–Si–Ni–Cr shape memory seamless couplings

I. Esquivel [a,b], J. Malarría [a,b], A.V. Druker [a,b,*]

[a] *Facultad de Cs. Ex., Ingeniería y Agrimensura (UNR), Av Pellegrini 250, Rosario, Argentina*
[b] *Instituto de Física Rosario (CONICET-UNR), Bv. 27 de Febrero 210 bis, Rosario, Argentina*

ARTICLE INFO

ABSTRACT

The Fe–Mn–Si shape memory (SM) alloys have attracted a great deal of interest due to their good technological characteristics and mechanical properties, combined with the SM effect. They are especially useful for applications like shaft and pipe couplings. In this work, we present the development and evaluation of a procedure to manufacture SM seamless couplings. After analysing industrial forming methods, we designed and fabricated a prototype of a punch-extrusion (PE) die and obtained seamless tubes of satisfactory quality and length for manufacturing couplings. Finally, we measured the performance and SM properties of the PE couplings and compared these characteristics to those of couplings machined from a cast ingot. We concluded that a multi-step processing is an efficient solution that mitigated problems resulting from billet cooling during punching because it allows the alloy to be reheated. The PE couplings that were diametrically expanded 4% and annealed at 700 °C exhibited 75% shape recovery, while the control samples showed 20% less recovery. The union of 21 mm diameter shafts by means of PE couplings annealed at 700 °C showed 40 N-m/cm^2 normalized torque transmission, which was 25% greater than that found for the cast ingot couplings. We also analyzed the advantages of the PE couplings compared to a traditional shrink-fit connection.

1. Introduction

"Shape memory alloys are fascinating materials, with potential applications as "smart" and functional materials" (Otsuka and Wayman, 1998). In particular, these alloys are characterized by the shape memory effect (SME) and superelasticity (SE) behaviours, which are closely related to a reversible diffusionless martensitic phase transformation. Some low-cost Fe-based alloys show shape recovery through different kinds of martensitic transformations. In high-manganese Fe–Mn–Si alloys, the stable high-temperature austenite phase (γ, FCC) transforms to a plate-like ε-martensite (HCP) at room temperature. Transmission electron microscopy (TEM) observations show that pre-existing stacking faults in the austenitic matrix are sites for martensite nucleation. Very thin plates grow due to the gliding of Shockley partial dislocations on alternating {111} austenitic planes (Nishiyama et al.,1978). Sato et al. (1982) found that after deformation the original shape can be recovered by subsequent heating to certain temperatures, if the transformation is induced by an applied stress. These temperatures activate the reverse transformation.

The Fe–Mn–Si SM alloys are interesting for several important

reasons:

a) they have good technological characteristics – formability, weldability and castability – and mechanical properties, i.e., toughness, high strength and fatigue behaviour.
b) they are much cheaper than other SMA, such as the Ni–Ti type.
c) the γ → ε martensitic transformation is induced at room temperature, simplifying the handling of the material.

These characteristics combined with the SME are especially useful for the development of technological applications like unions for crane tracks, joints for construction of curved structures, seismic dampers for buildings, and shaft and pipe couplings, among many others (Sawaguchi et al., 2016).

It is well known that the SM properties are mainly affected by the texture and the microstructure of the austenitic grains, and these conditions depend on thermo-mechanical treatments (Stanford and Dunne, 2006). More than ten years ago, Baruj and Troiani (2008) and Druker et al. (2010) found an almost perfect SME in Fe–Mn–Si-based alloys after an appropriate combination of rolling at an intermediate temperature

---

followed by annealing. According to Peng et al., 2018, the requirements to achieve large recovery strains in polycrystalline Fe–Mn–Si based SMAs are, firstly, a stacking fault energy (SFE) lower than 12 mJ/m^2 – which depends on the chemical composition (Li et al., 2000) and the temperature (Lee and Choi, 2000). And secondly, a sufficient density and distribution of crystalline defects – a high density of stacking faults uniformly distributed in the austenitic matrix (Kajiwara, 1999), dislocations (Baruj and Troiani, 2008), interstitial atoms (Tsuzaki et al., 1992) and a dispersion of precipitates (Kajiwara et al., 2001). Wen et al. (2014) found that these microstructural features strengthen the austenitic matrix and suppress annealing twins. Recently, Esquivel et al. (2019) investigated the effect of chemical composition and thermomechanical treatments on the mechanical properties and the SM capacity of two Fe-based SM alloys. Our results showed that the Fe–17Mn–6Si–10Cr–5Ni alloy rolled at 1000 °C and annealed at 700 °C exhibits the highest DSR, i.e. 78%.

Keeping in mind potential industrial applications, such as structures, couplings for shafts and pipes, actuators, and other devices, our group has been investigating Fe–Mn–Si–Cr–Ni SMAS for many years, obtaining interesting results (Druker et al., 2012). Couplings are one of the more promising applications, particularly when replacing traditional techniques that are difficult to apply in specific situations or modern techniques that are expensive and need sophisticated equipment. According to Marré et al. (2010), nowadays, manufacturing of heat exchangers, camshafts, intermediate shafts or cylinder liners is done using die-less hydroforming. This process, also known as hydraulic expansion, seems to be an interesting alternative to conventional welding and riveting. New developments in boss forming of tubes combined with a proposal to join tubes to sheet using a new room-temperature forming process have been made by Alves et al. (2018). Recently, Weber et al. (2021) published an interesting review about joining by forming. They analyzed the widespread demands that cause difficulties for commonly used joining technologies and introduced a variety of processes for joining by profile forming sheet-, bulk-, and sheet-bulk-components. Among other techniques, electromagnetic forming (EMF), die-less hydroforming, and incremental tube forming (ITF) are described and criticized. The temperature inside the joining gap during the collision process and its influence on the jet and cloud of particles is an important point with respect to EMF. Die-less hydroforming enables the establishment of force- and form-fit joints. Similar to EMF, the focus of investigations is the design of the forming zone. With respect to the ITF process, authors have affirmed that, while the establishment of a viable joint relies on elastic-plastic deformation, joining pressure must also be applied by an additional incremental tube forming tool. The establishment of material clearances needs to be analyzed, considering elevated temperatures, increased pressure, and different material combinations. For sheet joining, the processes of vaporizing foil actuator welding, roll cladding and in-situ hybridization of fiber metal laminates were also introduced by Weber et al.

Unfortunately, many authors have not taken into account how effective joining could be based on the shape memory effect. After investigating the industrial developments and current patents from several countries, Druker et al. (2014) designed an innovative coupling fabrication process based on forming and welding a rolled sheet. We manufactured prototypes and evaluated the shape recovery and the torque transmission capacity for 21 mm diameter shafts. The couplings showed good mechanical and SM behaviour. However, welding decreases the shape memory effect by 15% because of the heat-affected zone. Also, a geometric deviation from cylindrical symmetry must be resolved. We analyzed these weaknesses and paid special attention to the SM requirements described above. This study resulted in a method to manufacture 1 mm thick seamless couplings to join 21 mm nominal diameter shafts.

Here, we compare the performance of the new seamless couplings to those previously fabricated by welding. There are a number of industrial methods to manufacture seamless tubes from a cylindrical billet. In case of steel, the Mannesmann process is typical and the most economic (Dieter, 1961). But other methods are more appropriate to obtain small parts (Giotti et al., 2009). Punching is a simple operation that consists of applying a force through a punch to penetrate a billet contained in a die. The average degree of deformation is equal to $r = \frac{d}{D}$, where d is the punch diameter and D the external diameter of the raw billet. The larger the punch size, the greater the dimensional change that can be obtained, but the more difficult the operation because of edge effects and material hardening. Another method is extrusion, which is especially suitable for soft metals, as recently shown by Sivasankaran et al. (2021). Extrusion is a compression process in which the working metal is forced to flow through a die opening to produce a desired cross-sectional shape. Direct or indirect extrusion can be performed as a continuous or a discrete process, and it is affected by the working temperature, in other words cold, warm, or hot extrusion. Depending on the value of r, the material's flow geometry and the billet's deformation have particular characteristics (Comaneci et al., 2015). When $r < 0.3$, the billet deforms slightly on the surface at the moment the punch contacts it, and then the operation continues in a stationary state until it reaches a maximum depth. In this way, a central hole is produced with little geometrical deformation. This procedure is called *piercing*. When r is > 0.3, the surface deformation is greater and the billet is crushed, as the tip of the punch is forced to penetrate the material. This is the case for indirect extrusion. The upsetting stage only occurs if the initial billet diameter is smaller than the inside diameter of the die. When no upsetting is observed, the operation is completely extrusion. Usually, the procedures to obtain tubes are called *backward tube extrusion* and *forward tube extrusion*. For short or medium length products, the most practical arrangement is along the vertical work axis. Working in several stages or steps (*multistage manufacturing*) is recommended in order to achieve finite deformations or for hard materials, thus distributing less severe deformations over multiple steps.

In this work, we discuss the fixturing design, conduct calculations, and show the equipment fabrication and instrumentation required to perform punching, which is one type of a forging operation, combining with extrusion. With this technique, we manufactured seamless couplings of Fe–17Mn–6Si–10Cr–5Ni alloy, employing a specially designed die, thus creating prototypes. Finally, these were compared to a control sample, a coupling machined from a circular-section ingot.

2. Experimental methods

The Fe–17Mn–6Si–10Cr–5Ni SM alloy (nominal composition) was prepared in an induction furnace operating at 10 KHz and 30 KW. Commercial raw material was melted in high-purity alumina crucibles and cast into 34 mm diameter cylindrical moulds, providing a shape suitable for punching. The ingots were homogenized at 1150 °C for 3 h.

The ingots were formed into tubular parts using a 400 kN hydraulic press and a custom process. The working temperature was 1250 °C. For characterization, the tubes were cut into annular samples by electric-discharge machining, and then annealed at different temperatures between 700 and 1000 °C for 30 min. The nomenclature to identify the samples is simple: **PE** plus the annealing temperature (for example **PE700**).

To evaluate the SM behaviour, the diameter was measured before and after the couplings had been expanded by a special device from ϕ_{man} to ϕ_{exp}, and after subsequent annealing at 500 °C for 5 min to activate the reverse transformation to diameter ϕ_{ret}. The degree of shape recovery, DSR_C, was calculated as:

$$DSR_c = \frac{\varnothing_{exp} - \varnothing_{ret}}{\varnothing_{exp} - \varnothing_{man}} \cdot 100 \qquad 1$$

The elastic expander, subdivided into segments or pins (Fig. 1a), was inserted into the pierced billet (coupling or ring). The segments were then expanded in the radial direction by the action of a conical punch
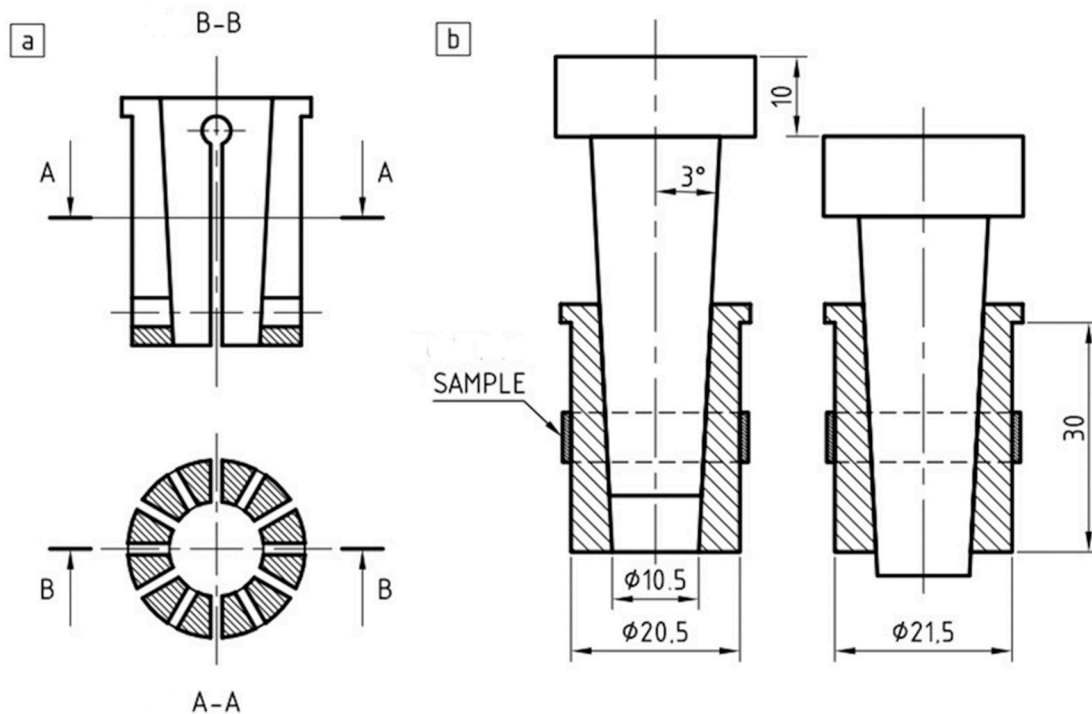
Fig. 1. a) Elastic expander for couplings and rings. b) Operational diagram and general dimensions.

(Fig. 1b), forcing the diametrical expansion of the part. Ideally, the circumferential stresses are distributed homogeneously along the perimeter of the coupling, thus promoting homogeneous deformation. Due to the limitations that restrict the number of possible cuts, we settled on 12 subdivisions. Molybdenum disulphide lubricant was applied on the entire surface (external and internal) of the expansion tool, on the punch, and on the internal surface of the couplings.

The load on the punch was applied using an Instron 3382 testing frame, while the force and the punch displacement were recorded using the Bluehill II software. To control the deformation of the sample, we periodically measured its outer diameter during the expansion process.

To test the functionality of the couplings, two 21 mm diameter shafts were joined and the maximum transmitted torque measured. After assembly with the minimal clearance, the shaft-coupling-shaft set was heated inside a tube furnace to activate the reverse transformation to austenite. During air cooling, an interference fit between parts was
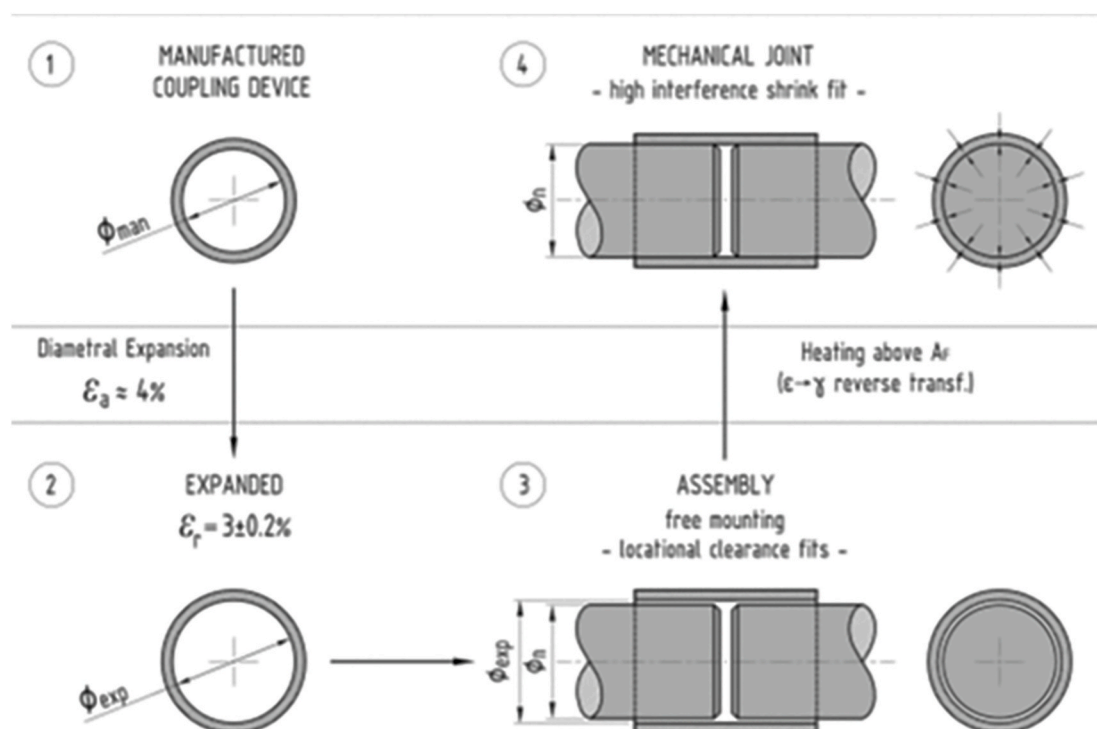

Fig. 2. Graphical illustration of the process to establish the shape memory coupling.

obtained. After cooling, one of the shafts was clamped in a vise, and a load applied to the other shaft with a torque wrench. The torque was progressively increased and recorded until slippage occurred.

The microstructure was examined using an Olympus PME3 optical microscope equipped with a Nomarski Interference Contrast (NIC) device. Specimens were mechanically polished to 1200 grit emery paper. In order to improve the surface finish, the last step was an electrolytic polish using a solution of 80% acetic +20% perchloric acid at 27 V for 60–90 s. This procedure has the additional advantage of revealing the austenite grain boundaries.

3. Dimensional analysis of shape memory couplings

The correct sizing of the manufactured SM couplings is critical in order to obtain efficient mechanical joining. The coupling system and how it is used (shown in Fig. 2) impose several conditions that must be taken into account:

1. The manufactured internal diameter ($\varnothing_{man}$) must be less than that of the element to be joined (shaft, tube, etc);
2. The coupling must be expanded to induce martensitic transformation, up to an internal dimension, $\varnothing_{exp}$;
3. In this expanded state, the coupling is mounted over the elements to be joined (the locational clearance must be a minimum in order to improve the final interference fit);
4. Joining of the parts is produce by shape recovery after heating to above the A_F temperature. The greater the interference fit reached, the greater the strength of the joint.

The objective of this section is to define the following dimensions of the coupling system:

- $\varnothing_{man}$: Internal diameter of the manufactured coupling device, with corresponding tolerance.
- $\varnothing_{exp}$: Internal diameter of the expanded coupling device after elastic plus pseudoelastic relaxation, with the corresponding tolerance.
- I_{max}; I_{min}: Maximum and minimum geometric interference between the coupling and shaft, after the reverse transformation.

The calculation of these dimensions depends on different technological parameters, which in our case take the following values:

- $\varnothing_n$, tube or shaft nominal diameter = 21 mm
- ε_a, the diametral expansion strain applied to induce the martensitic transformation = 4%. This value was selected based on previous experience.
- ε_r, the diametral remnant strain (measured after elastic and pseudoelastic recovery) = 3 ± 0.2%.
- DSR_d, the expected degree of diametric shape recovery = 74 ± 4%.
- an estimate of the desired fit between the parts, which can be expressed as geometrical interference.

Before calculating the coupling dimensions, the maximum and minimum possible dimensions of the elements to be joined must be known (that is, a nominal value and dimensional tolerance). In our case, we decided to manufacture couplings for joining 21 mm nominal-diameter shafts (or possibly tubes). Such shafts can be made from drawn or rolled bars. The bars are manufactured with a base shaft tolerance, which means that the maximum possible value coincides with the nominal value, and the entire tolerance range includes smaller shaft diameters. Table 1 summarizes the tolerances reported by a shaft supplier Arcelor Mittal.

We begin by considering the mounting condition (step 3 in Fig. 2), in which the expanded coupling device must be located on the shaft (s) with a minimum clearance fit. To address such a condition, we used the dimensions recommended in the ISO 286-1: 2010 standard. For rough

Table 1
Shaft tolerance range for standard materials and processes.

Processing	Tolerance category	Tolerance range for $\varnothing_n$ = 21 mm
Drawn	h11	+0 − 0.130
Hot rolled	h12	+0 − 0.210

adjustments with clearance and free mounting on the single shaft system, the following categories are recommended: C11h11, D9h9, F8h7, and the subsequent ones for reduced clearance and tighter tolerances. C11h11 is the loosest fit recommended. In this case, the tolerances are coarser (h11 and h12), and therefore, we will use the recommended clearances as a reference to establish the assembly condition in view of the minimum achieved clearance. We selected F11h11 and F11h12 fits, which specify a minimum clearance of 0.020 mm. This is enough to permit a simple assembly without difficulties. We believe that it is unlikely we will achieve this minimum clearance. The gap will usually be higher. On the other hand, the clearance should not be excessive because it reduces the efficiency of the reverse-transformation fit. The clearance ranges of the adopted fits are shown in Table 2, and the mounting condition (in the case of a drawn shaft) will be shown graphically in Fig. 16a. In this case, the dimension of the expanded coupling becomes:

$$\varnothing_{exp} = \varnothing21F11 = \varnothing21^{+0.150}_{+0.020}mm$$

We now calculate the as manufactured dimension $\varnothing_{man}$ (step 1 in Fig. 2), considering a remnant strain in the diametric expansion: $\varepsilon_r = 3 \pm 0.2\%$.

The maximum expanded diameter, $\varnothing_{exp.max.}$, will occur when the maximum degree of expansion is applied to the maximum manufactured diameter ($\varnothing_{manmax}$).

$$\varnothing_{expmax} = \varnothing_{manmax}(1 + \varepsilon_{r\ max}) \qquad 2$$

$$\varnothing_{manmax} = \frac{\varnothing_{expmax}}{1 + \varepsilon_{rmax}} = \frac{21.150}{1.032} = 20.494mm$$

Similarly,

$$\varnothing_{manmin} = \frac{\varnothing_{expmin}}{1 + \varepsilon_{rmin}} = \frac{21.020}{1.028} = 20.447mm$$

Then, the resulting manufactured internal diameter ($\varnothing_{man}$) is

$$\varnothing_{man} = 20.4^{+0.094}_{+0.047}mm$$

The dimension calculated for the coupling's internal diameter corresponds to ø20.4E9. The IT9 degree of tolerance was perfectly achieved by lathe turning (Oberg et al., 2004). This was the last manufacture step.

The next requirement was to determine the interference after the reverse-transformation. This gives the in-service operating condition for the coupling (step 4 in Fig. 2). We analyse what would occur for a free reverse-transformation (without restriction) using the measured DSR_C values and their associated error (see Section 5.2.1). The diameter after the reverse transformation ($\varnothing_{ret}$) is calculated using Eq (1),

Table 2
Fit tolerances to assemble the coupling and the range of corresponding clearances.

	Fit conditions for assembly	Minimum clearance (mm)	Maximum clearance (mm)
On a drawn shaft	Ø21 F11 h11	0.020	0.280
On a rolled shaft	Ø21 F11 h12	0.020	0.360

$$DSR_C = \frac{\varnothing_{ret} - \varnothing_{exp}}{\varnothing_{exp} - \varnothing_{man}} = 74 \pm 4 \ \%$$

$$\varnothing_{retmax} = \varnothing_{expmax} - DSR_{Cmin}\left(\varnothing_{expmax} - \varnothing_{manmax}\right) \qquad 3$$

$$\varnothing_{ret\,min} = \varnothing_{exp\,min} - DSR_{C\,max}\left(\varnothing_{exp\,min} - \varnothing_{man\,min}\right) \qquad \text{Eq 4}$$

Substituting values gives:

$$\varnothing_{retmax} = 20.690 mm$$

$$\varnothing_{retmin} = 20.573 mm$$

In this state, maximum and minimum interferences are:

$$I_{max} = \varnothing_{shaftmax} - \varnothing_{retmin} = 21.000 - 20.573 = 0.427 mm \qquad 5$$

which is valid for both a drawn and a rolled shaft, since the upper dimension is equal to the nominal size, as shown in Table 1. The minimum interference will depend on each material:

$$I_{min} = \varnothing_{shaftmin} - \varnothing_{retmax} \qquad 6$$

$$I_{min}(drawn) = 20.870 - 20.690 = 0.180 mm$$

$$I_{min}(rolled) = 20.790 - 20.690 = 0.100 mm$$

These interferences (shown graphically in Fig. 16b for a drawn shaft) result in an extremely tight fit in comparison to the mechanical fits suggested by the Standard. It is difficult to determine what would be the fit between the shaft and the retransformed coupling in terms of the Standard. The lower rows in Table 3 show dimensions for a standard non-shape-memory material system closer to what could be achieved for SM couplings. For this, the ZC category was used because it is the furthest from the nominal dimension and, even so, the interference is lower than what can be achieved by the retransformed coupling. This difficulty is logical since it is almost impossible to assemble the coupling and shaft with such a level of interference, even if the two parts were made from standard materials (for example steels) and the coupling is heated and high assembly pressures applied. The result of the attempted assembly would be damage to the shaft and coupling. Therefore, the standard does not apply in these situations. In contrast, in the case of SM couplings, the assembly is carried out in a "free" or sliding condition, as stated above. Then, the retransformation is carried out once the coupling is mounted on the shaft, so that a high level of interference is achieved without difficulties in assembly.

4. Design of the coupling manufacturing process and forming devices

The couplings are fabricated from a billet cut from a cylindrical ingot. It is extremely difficult to achieve a 1 mm wall thickness in a single forming operation. Thus, the manufacturing process is performed in two stages. The first one involves the production of a hollow part, called a *preform*. This preform is then lathe turned, the second operation, to generate the final dimensions of the seamless coupling. The material sizes of each stage are shown in Fig. 3. One important parameter is the

Table 3
Interference ranges achieved after the reverse-transformation. The equivalent ISO Std system fit is included.

	Fit after reverse transformation	Minimum interference (mm)	Maximum interference (mm)
On a drawn shaft		0.180	0.427
On a rolled shaft		0.100	0.427
ISO Std.	Ø21 ZC12 h11	0.050	0.398
	Ø21 ZC12 h12	−0.022 (clearance)	0.398

extrusion ratio (also called the reduction ratio), $R = \frac{A_0}{A_f}$, where A_o is the cross-sectional area of the starting billet, and A_f, the final cross-sectional area of the extruded section (A_B and A_{HP}, respectively, are indicated in Fig. 3). We also calculated the percentage reduction, RD. Thus, these parameters become

$$RD(\%) = \frac{A_B - A_{HP}}{A_B} 100 \qquad .7$$

$$R = \frac{A_B}{A_{HP}} \qquad 8$$

To obtain the hollow preform from this hard alloy, we analyzed many parameters: the working temperature, the heat loss due to contact with the die and punch, the loading speed, friction and lubrication, among others. The analysis of the different alternatives led us to select a *Multistage punching and direct extrusion* process (PE). Kajikawa et al. (2021) have recently shown a stepped method for forming an extremely deep cup from aluminum alloy sheet. Compared to other options, the lower frictional resistance of their process reduces the workload and pressure between the parts. Less workload means lower required force capacities and a less compromising device design. Additionally, lower pressure between work surfaces reduces the heat loss from the material. A multi-step operation allows for the cooled and hardened billet material to be reheated, and for the die and punch to be re-lubricated.

Each step begins when the hot material is introduced into the die, and finished when no punch displacement is register although the load increases. This point probably matches the cooling and hardening of the material to a point which will not permit more deformation, for the given geometric conditions. In addition, each step includes the monitoring and recording of the test parameters. Between steps, the preform and the matrix are reheated so that the temperatures are the same at the beginning of each new step.

4.1. Design and manufacturing of the devices

The main dimensions of the die and the manufactured assembly (in section view, for better visualization of the inner geometry) are shown in Fig. 4a and b, respectively. The die confines and contains the starting material blank. It is open at the top to feed the material and introduce the punch, and also at the bottom to allow for the maximum punch stroke. The die consists of several removable pieces in order to facilitate material extraction in case of jamming. The removable design also allows for internal inspection of the matrix to evaluate wear or possible material binding. In selecting the steels for fabricating each part, we accounted for specific requirements. The materials used are indicated in the caption of Fig. 4b, according to SAE Standards. In particular, we selected H13 steel for the split die and punches, which will be subject to wear and high temperature, see Wick et al. (1984) who recommended this steel for the construction of extrusion dies.

The split die is made of two equal and symmetric pieces and is closed (both halves together) by the action of two flanges, adjusted by four studs. To achieve an effective and tight seal, the mounting surface is designed with a dual tapered geometry. By adjusting the studs that close the assembly, the die is subjected to perimeter compressive loads, which oppose the tensile loads developed during the punching operation (Schuler GmbH, 1998). The lower flange acts as a support base for the device. In accordance with Zhoua et al. (2020), to achieve a relatively large and homogenous effective strain in the cross-section, the interior of the die was machined with a 4° half-angle to form a conical housing (Fig. 4a). The conical housing solves in a practical way the problem associated with expansion at the moment of introducing the hot billet (or preform) after each reheating step. As the housing expands, its dimensions increase, but it maintains the taper. Therefore, it will rest appropriately on the conical surface of the die, remaining a little higher or lower depending on the degree of expansion, but the preform will
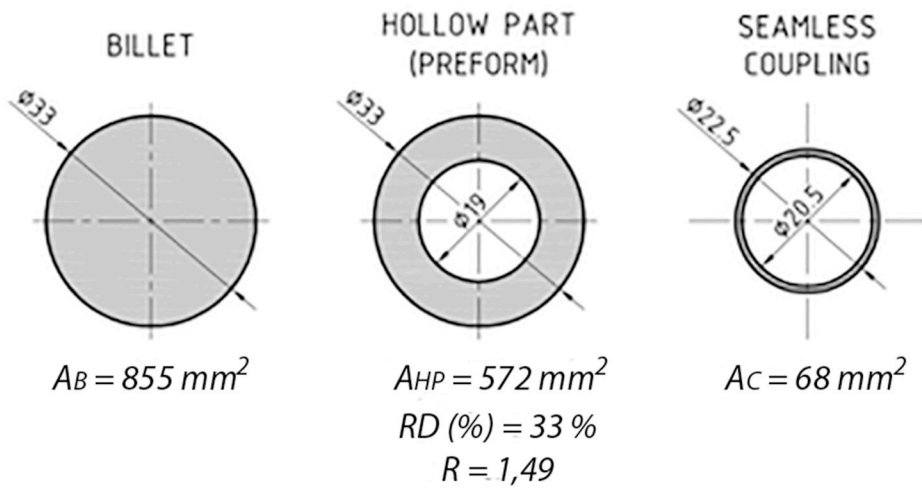
Fig. 3. Dimensions and section areas of: a) the billet, b) the hollow preform, and c) the seamless coupling.
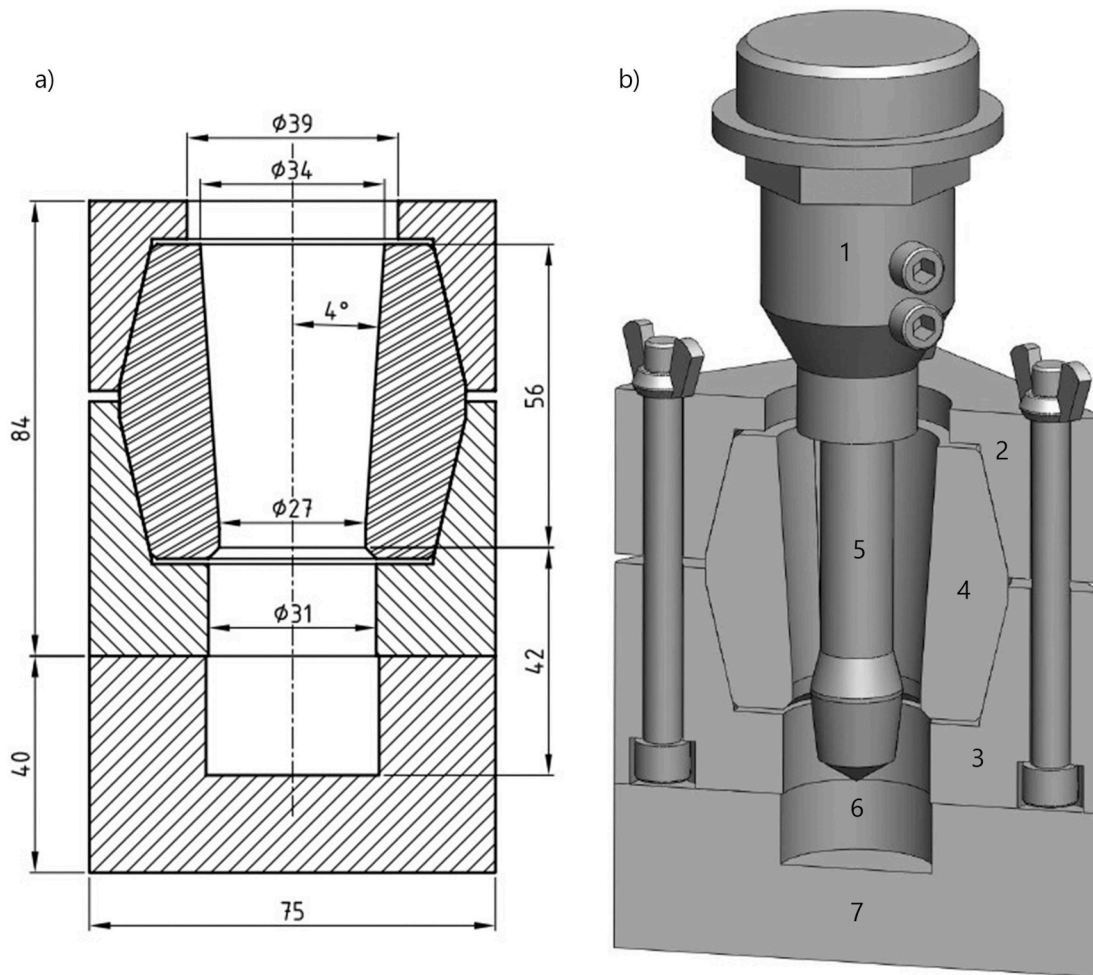

Fig. 4. a) Schematic drawing of the die, b) Features of the entire assembled system. 1- sleeve bearing (SAE 1020), 2- upper flange (SAE 1045), 3- lower flange (SAE 1045), 4- split die (H13), 5- punch (H13), 6- relief space, 7- auxiliary support base (SAE 1045).

always be centred and enter without difficulty.

The punches are distinguished by three different zones, as shown Fig. 5:

- Zone 1: conical tip

- Zone 2: calibrated diameter (maximum punch diameter)
- Zone 3: Relief zone (reduced punch diameter).

Before completely traversing the billet, the punch must be withdrawn upwards at the end of each deformation step. During these first
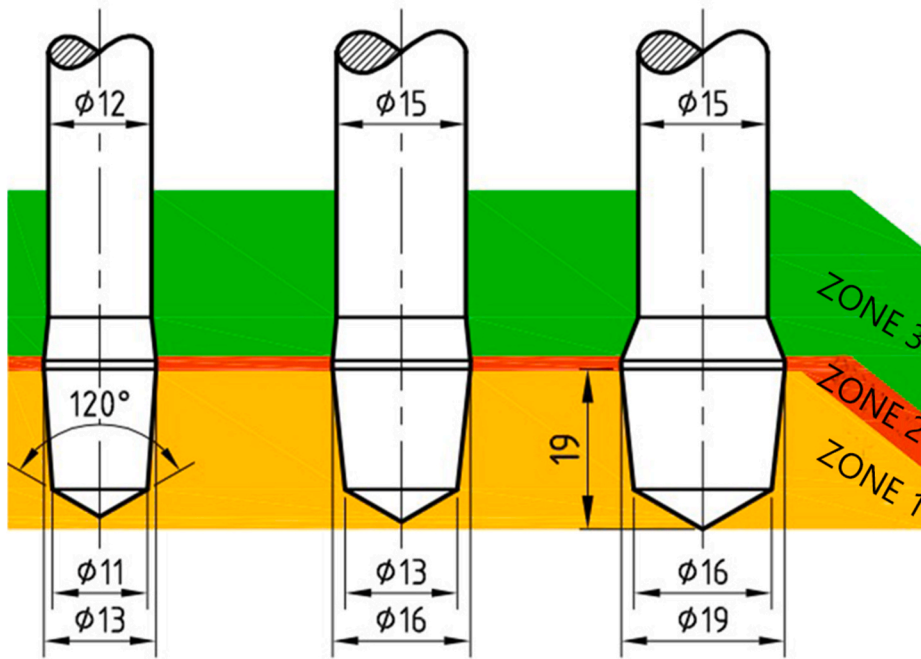
Fig. 5. Series of different sized through punches used to manufacture seamless couplings.

steps, the conical profile of zone 1 will be essential to uncouple the punch and part without complications.

4.2. Equipment and lubrication

The force required for the punching-extrusion (PE) operation was provided by a 400 kN hydraulic press controlled by the corresponding instrumentation. The details characterizing this equipment, its operation and how it was instrumented are summarized in Appendix 1. Additionally, we used separate muffle furnaces with 1100 and 1250 °C temperature capabilities for heating the die and the billet, respectively.

Kumar et al. (2014) summed up the importance of lubrication: 1) necessary to reduce the friction coefficient between the working surfaces, thus promoting "smooth" material flow during deformation, 2) will form a separation layer between the billet, die and punch to avoid welding, and 3) facilitates the extraction of the part. New methods for determining the friction in the forming of complex parts are presented, such as the one recently discussed by Hu et al. (2017). We decided to use a water-based, non-graphitic, commercial hot forging lubricant, "Qua-forge 650", produced by Quaker Chemical Co. It was applied with a hand spray to the entire internal surface of the die, before inserting the billet or preform, and also to the punch tip just before the working stroke began. This lubricant remains in a liquid state up to high temperatures. As the aqueous base evaporates in only a few seconds, the lubricant dries leaving a dispersed solid remnant, similar to ash, which enables separation of the die components and facilitates billet extraction.
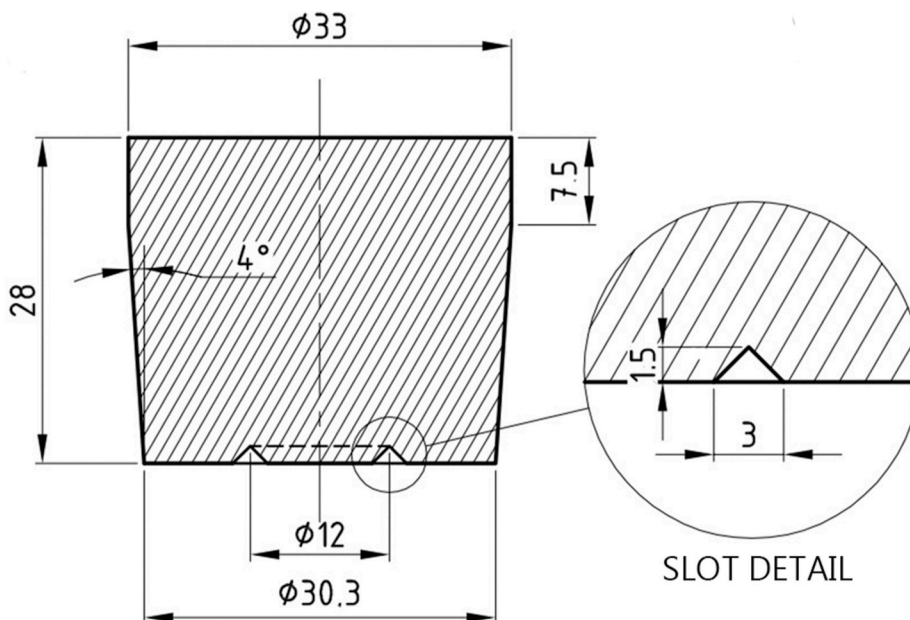

Fig. 6. Dimensions of the slotted billets.

4.3. Raw material preparation: geometry and sizing of the billets

As mentioned above, the ingots were chopped and machined into billets to begin the fabrication of the seamless couplings. Firstly, the billets were turned to the same conicity as the die housing. Easy material separation at the exit of the punch can be obtained from a certain state of stress, such as that resulting from a stress-concentrating groove in the base of the billets. Therefore, we prepared a series of slotted billets and compare the effect against unslotted ones. Dimensions are shown in Fig. 6.

4.4. Calculation of the punching force and maximum support load

To verify the applicability of the devices (dies, punches and auxiliary elements) and the capacity of the loading frame and the hydraulic actuator, we calculated the necessary force for punching, F_P. This design assumes that the billet, being "held" by the conical housing of the die (Fig. 7a), is deformed at a working temperature by the action of the punch. The support capacity of the conical housing is represented by force F_s, which is the result of the vertical components of the normal pressure and the frictional resistance developed on the contact surface between the billet and the die (Fig. 7c). Since F_s is a reaction force, the equilibrium condition ($F_s = F_P$) is fulfilled at every moment. Potentially, the punching force can grow up to a critical value at which the support load F_s attains its maximum (i.e., the static friction condition no longer exists). This critical value is denoted as F_C, the maximum support load. When this situation is reached (Fig. 7b), the punching to a tubular geometry ceases. Instead, the punching load creates the sliding and extrusion of the billet (or preform) from the die. The calculation of F_C is helpful in designing the taper angle, α, in order to avoid this undesirable situation.

The calculation of F_P and F_C is based on traditional mechanical engineering techniques (Dieter, 1961; Schuler GmbH, 1998; Groover, 2010), where the load necessary for a certain operation is obtained as a function of the extrusion ratio R (Eq. (8)). Considering both the forming and frictional work for this particular forming operation, we found the following expressions (the complete derivation is included in Appendix 2):

$$F_p(y) = \sigma_f \frac{\pi}{4} \left(\varnothing_0^2 \ln R_p + 0.3 \left(\varnothing_{P_0}^2 + 4 \varnothing_{P_0} y \right) \right) \ \forall \ y > 4 \qquad (9)$$

$$F_c = \sigma_f \frac{\pi}{2} \varnothing_0 l_0 \left(\frac{\varnothing_0}{2} \ln R_s + 0.6 \right) \qquad (10)$$

where $\varnothing_0$ and l_0 are the initial diameter and the initial length of the billet, respectively, $\varnothing_{P_0}$ is the diameter at the top of the punch, and α and β are the taper angles of the die housing and the punch head, as shown in Fig. 7. One should note that σ_f is the alloy's yield stress at the working temperature.

Calculating R_p and R_s, the extrusion ratio in punching and sliding, respectively, are:

$$R_p = \frac{\varnothing_0^2}{\varnothing_0^2 - \left(\varnothing_{P_0} + 2 \left(y - 4 \right) \tan \beta \right)^2}$$

$$R_s = \frac{\varnothing_0^2}{\left(\varnothing_0 - 2 \tan \alpha \right)^2}$$

After making the calculations for different combinations of geometrical parameters (i.e. evaluating the taper angle, α, assigned to the billet housing) we adopted the following dimensions in our design: $\varnothing_0 = 33 \ mm$, $\varnothing_{P_0} = 16 \ mm$, $\alpha = 4°$, $\beta = 6°$.

The corresponding values of F_P and F_C, as a function of the stroke y, are plotted in Fig. 8. The punching force increases with penetration depth. The rise is fastest at the beginning of the operation due to the 120° tip angle of the punch, up to the diameter $\varnothing_{p0}$ (this corresponds to a depth of approximately 4 mm). In order to simplify Eq. (9), we presented an expression valid only for y > 4 mm. From that point, the load grows linearly. It can be seen that during the working stroke the maximum support load is not reached for any of the billet's initial lengths.

The model employed for these calculations simplifies the real situation in several ways. It is assumed that:

- the strain is homogenous over the volume affected during each working stage,
- the temperature is the same throughout the preform (no temperature gradients are considered),
- the effect of friction is approximated by a constant value independent of the normal pressure between the contacting surfaces (and only proportional to the contact area of those surfaces). Following Dieter (1961), we considered the shear stress at the interface to be equal to the shear strength of the metal in plain strain. This stress was
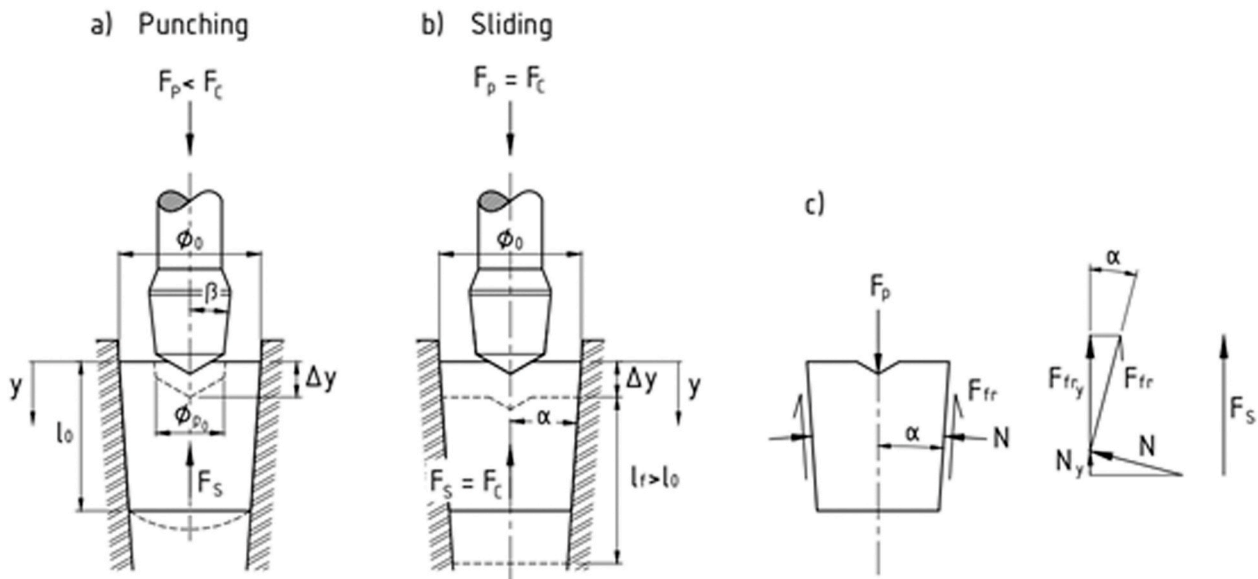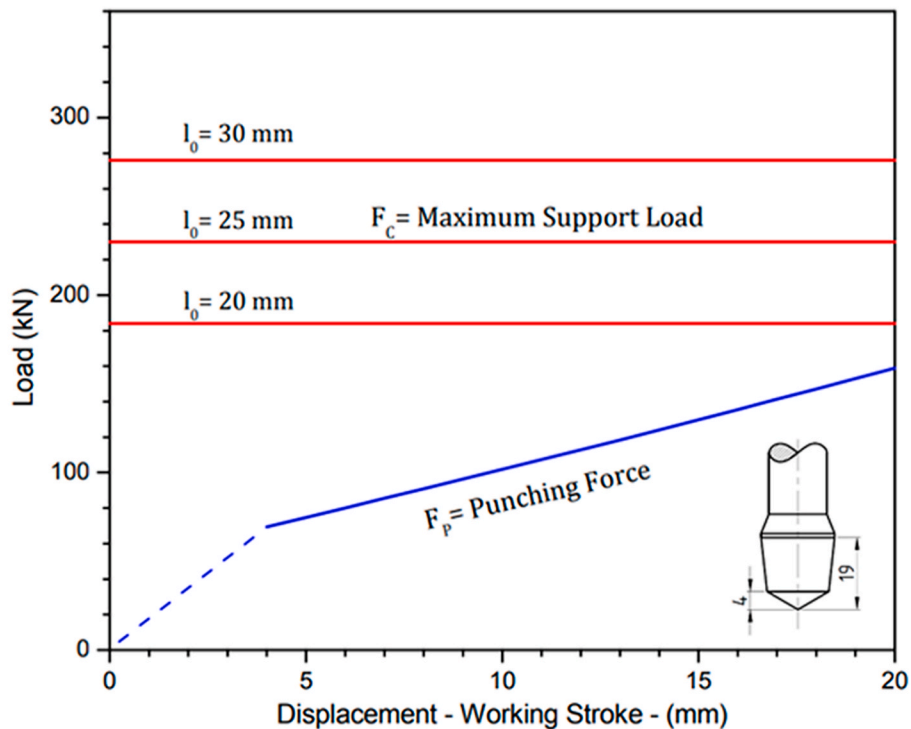

Fig. 7. Illustration of the variables and considerations for the calculation of forces. a) Penetration of the billet (punching) by the action of the external load. b) Displacement and extrusion of the billet in the die without punching. c) Free-body diagram considering the main forces, and their proportions along the *y* axis.

Fig. 8. Load-displacement chart calculated from *Eqs. 9 and 10*. The evolution of the punching load, F_p, and the maximum support load, F_c, for different initial lengths of the billet, l_0, are shown.

weighted by a coefficient of 0.6, in order to better approximate the real situation (see Appendix 2 for a detailed description).

It is difficult to accurately include the effect of friction within the extrusion equations. Dieter (1961) presented various empirical models and formulas adapted to particular cases (such as those of Sachs, Avitzur, Kudo, and DePierre). We tried these models by adapting them to our case, and did not obtain good results. Thus, we took the estimates as described above, which are included in the formulation of *Eq. (9)* and *Eq. (10)*. According to these equations, friction has a stronger contribution than the forming resistance to the values of the calculated loads, i.e., in the case of F_C the relative weights are 0.78 and 0.22 respectively.

In light of considerations described above, this model does not pretend to be a detailed analysis of the strains and stresses involved in the process. Notwithstanding, the model does approximate the magnitude of the loads developed during the process, particularly the punching force. This was necessary in order to estimate the required load capacity of the mechanical testing frame and the necessary potential of the frame's hydraulics. The model also gives the maximum support load (to ensure punching of the preform without sliding). Thus, this modelling provides a useful general idea of the system performance for all of the forming stages. It should be noted that in the second and third forming stages smaller punches are employed. Because of this, the punching force is expected to be smaller, as well.

5. Results and discussion

5.1. Performance of the punching-extrusion system

5.1.1. Working conditions, procedure and prototypes

The operating conditions of the hydraulic equipment and the process variables are given in Table 4. Fig. 9 shows the evolution of the raw material billet prepared as indicated in Fig. 6; the billet's initial length and volume were 28 mm and 22.300 mm^3, respectively.

The hole is formed in the first steps, until the remaining material at

Table 4
Operating conditions of the billet piercing operation.

Initial dimensions of the billet	Ø 33 mm × 28 mm (Fig. 6)
Material heating temperature	1250 °C
Die heating temperature	450 °C
Header speed	5–6 mm/s
Lubricant	Quaforge 650
Punch diameters	Ø13 - Ø16 - Ø19 mm (Fig. 5)

the base of the preform no longer resists the action of the punch. At this point, the material ruptures and the base opens. In subsequent steps, with changing to calibrated larger-diameter punches, the inside diameter of the hole is enlarged.

Preforms with a 19 mm final inner diameter are shown in Fig. 10. A zone of material rupture and detachment is observed at the base of the pieces made from billets without a groove (Fig. 10a). On the other hand, those preforms formed from slotted billets show a neat cutting surface. Because the groove acts as a preferential cutting area, perfect disks of material were detached. Even if the punch first pierces the centre of the piece, the groove impedes the radial propagation of cracks.

Once the part has been pierced, the passage of the successive punches (see Fig. 9) eliminates cutting defects by plastic deformation, and thus improves the surface and geometric quality of the pierced surface. Consequently, a high-quality cutting area is obtained, as seen in Fig. 10b. In short, we have obtained high geometrical and dimensional quality cylindrical perforations, in all of the manufactured parts.

In all cases, the outer shape of the punched preforms reproduced the inner geometry of the die, which has a 4° taper. A final machining operation was performed to reduce the wall thickness and achieve the specified dimensions of the final product. Couplings are shown in Fig. 11.

5.1.2. Load-displacement control

The load applied by the press header as a function of the penetration
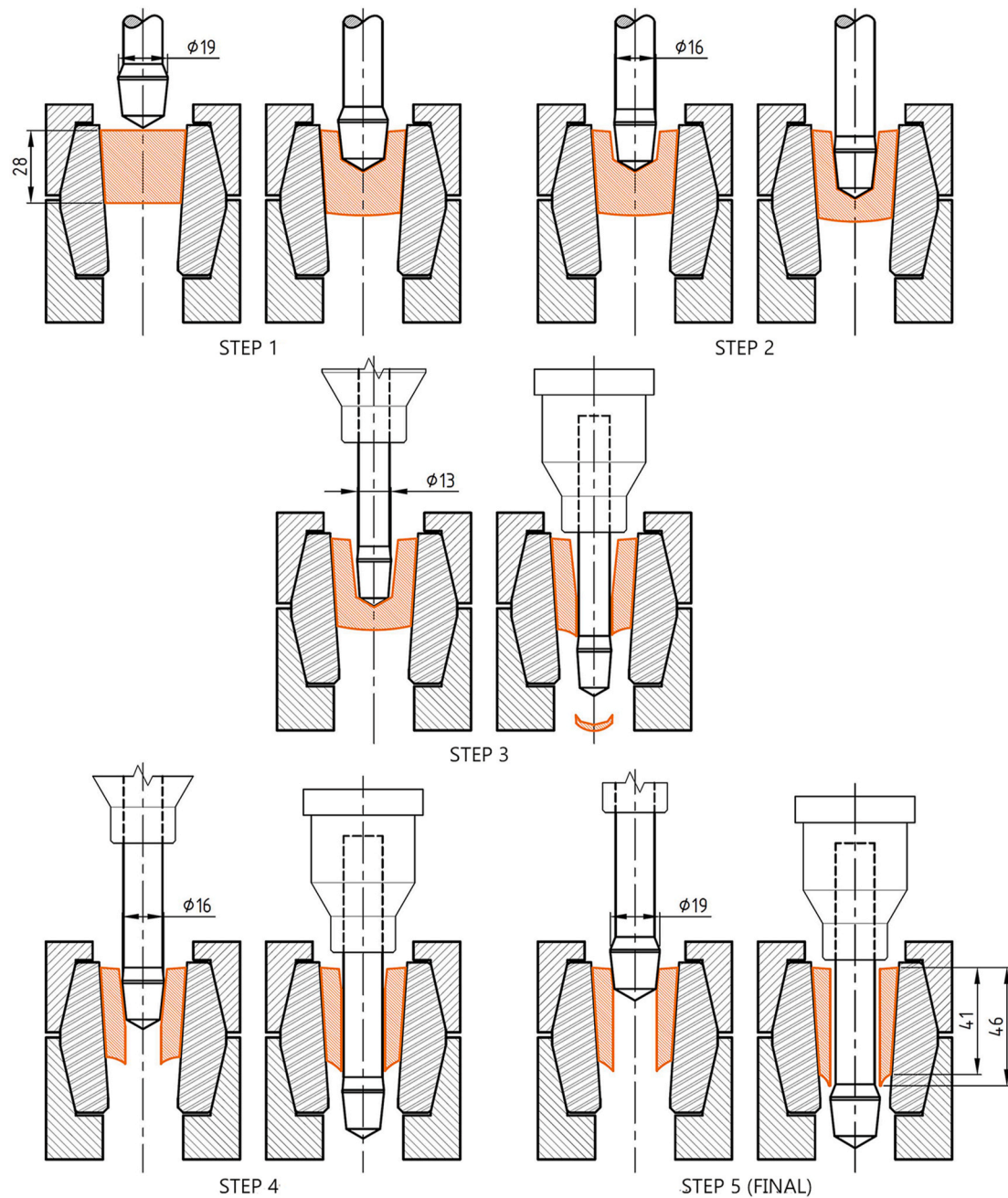
Fig. 9. Chart showing the forming steps to manufacture seamless couplings.

achieved in each forming step is shown in Fig. 12. The curves show the performance in each step of the completed forming process.

In the first two steps, the load increases rapidly with small punch displacements because the punch always finds material opposing its advance. Upon reaching each step's maximum penetration, the stroke is reversed and the punch extracted. These data are not included in the figure. It is important to note that the load levels recorded are similar to the values we calculated in section 4.4 (Fig. 8). The work piece is completely pierced after the third step, as shown in Fig. 9. In order to distribute the total work expended to complete these three steps, we divide the initial length of the billet (l_0) in three equal parts to set the maximum penetration of each step (this is $\frac{1}{3}l_0$ and $\frac{2}{3}l_0$ for the fist and the second steps respectively. The stroke of the third step is then what necessary to complete the piercing task). In the last two steps, the punches thin the wall of the already formed tube, and the total travel

equals the length of the preform. After the punch completely passes through the tubular geometry, it continues its advance towards the relief zone and the load drastically decreases.

5.2. Coupling performance

5.2.1. Degree of shape memory of couplings

We performed shape recovery tests on PE coupling samples and also on control samples obtained from the molten bar, using a special device described in Section 2. The degree of shape recovery (DSR_C), which depends on the remnant deformation as shown in Fig. 13, was calculated from Eq. (1). The SM behaviour degrades when the deformation increases in all cases, PE (Fig. 13a) and control specimens (Fig. 13b). Samples annealed at 700 °C showed better recovery than those annealed at 800 °C. Taking the coupling application into account, we paid specific

Fig. 10. Preforms obtained from: a) an unslotted billet, and b) a billet with a slot.

Fig. 11. Finished couplings, manufactured by PE and final machining.

attention to a 4% diametric expansion, which leads to a remnant strain of $\varepsilon_{rem} = 3\%$. Fig. 14 shows the degree of shape recovery of these couplings after annealing at different temperatures. Clearly, annealing at high temperatures (900 and 1000 °C) leads to the poorest shape recovery.

5.2.2. Coupling performance

To evaluate the performance of the SM couplings, two 21 mm semi-shafts were joined and the maximum transmitted torque measured. The $20.4^{+0.094}_{+0.047} mm \varnothing_{man}$PE and control couplings were expanded to $\varepsilon_{rem} = 3\%$. The length and the interior surface area were 19 mm and 6.1 cm^2, respectively. We proceeded as indicated in Section 2. When slippage began, the torque resistance drops and we removed the load. We consider that the maximum torque measured just before slippage, as the maximum torque that the joint can transmit. The results are shown in Table 5. For a better comparison, we define the *coupling resistance*, which was calculated as the maximum torque divided the contact area between shaft and coupling. PE couplings showed 30% more resistance when compared to the control samples. The last line in Table 5 shows the normalized torque transmitted by other 15Mn couplings manufactured by rolling and welding (Druker et al., 2014). This value was 50% lower
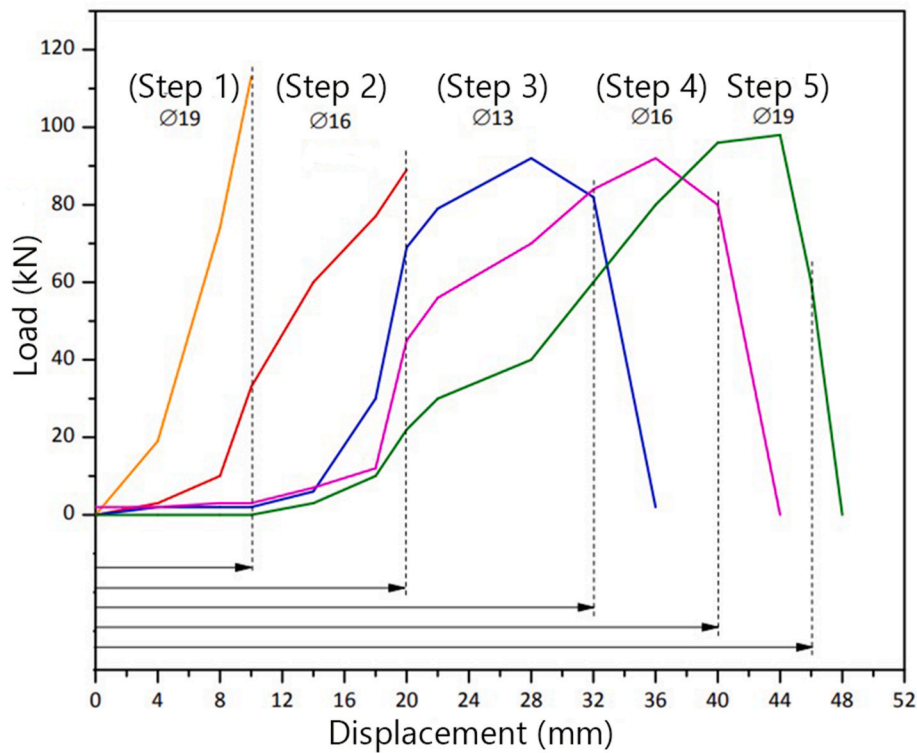
Fig. 12. Load-displacement curves for the seamless tube forming process. The initial billet was 28 mm high.
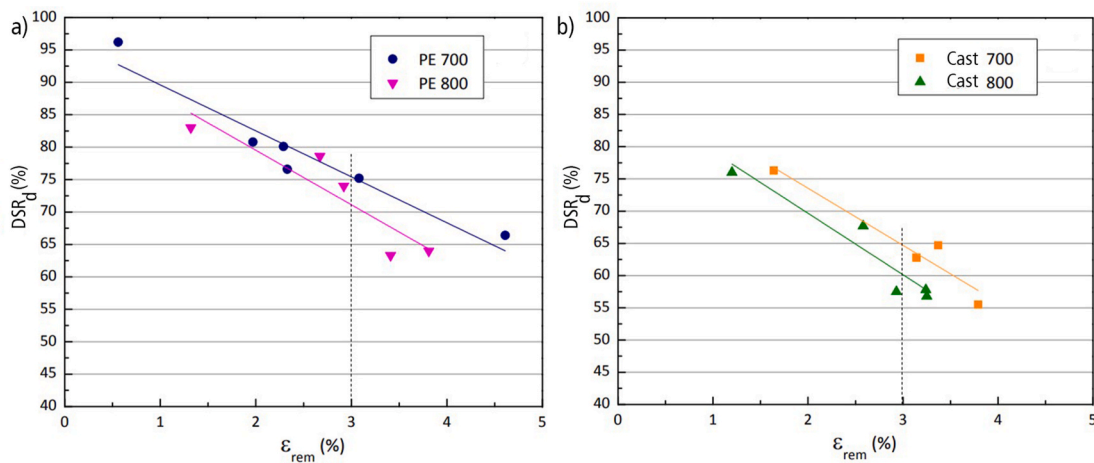

Fig. 13. Degree of shape recovery as a function of different remnant deformations.

than for the PE couplings.

5.3. Microstructural characterization

Although it was not one of the objectives of this work, we characterized the microstructure of the P-E couplings using optical microscopy. We created a cross section and analyzed the surface normal to the coupling's longitudinal axis, before and after applying a 4% diametric expansion in samples annealed at both 700 and 800 °C. The images in Fig. 15 show the full thickness in one area of the part with the inner diameter on the left and the outer diameter on the right-hand side of each image.

The austenitic grain size is approximately 100 μm for both annealing temperatures. The grains are not equiaxed, with the major axis in the circumferential direction and the minor axis aligned along a radial direction. With respect to grain size, it is possible that the successive preform heating steps, up to 1250 °C, activated grain growth, while the grains' geometry indicates that they were deformed due to compression in the radial direction. This would have resulted from forces exerted between the punch and the internal wall of the die.

No blocks or colonies of $Fe_5Ni_3Si_2$ precipitates are observed, neither inside the austenitic grains nor at the grain boundaries, as can be seen in Fig. 15a and c. This could be the result of the successive heating steps at 1250 °C, a much higher temperature than the stability range of these precipitates and sufficient for complete dissolution. Moreover, the subsequent annealing time was insufficient for new precipitation, at least that which can be observed on the optical light-microscope scale. Annealing twins appear clearly in the microstructures of both samples.

After the diametric expansion, ε-martensite plates were observed in the austenite grains, as shown in Fig. 15b and d. The plates appear with
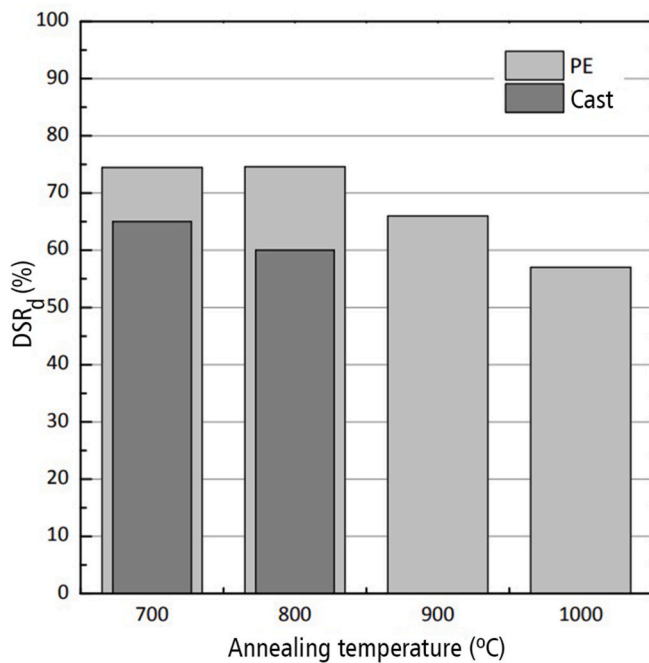
Fig. 14. Degree of shape recovery of couplings annealed at different temperatures, after 4% diametric expansion (ε_{rem}= 3%).

Table 5

Maximum torque transmitted and coupling resistance of SM couplings annealed al 700 °C.

	Max. Torque (Nm)	Coupling resistance (Nm/cm^2)
PE couplings	117	40
Cast couplings	88	30
15 Mn rolled and welded	–	21

only one variant per grain after annealing at 700 °C. However, two martensite variants developed in many of the grains of samples annealed at 800 °C. The curved appearance of these plates is characteristic of strain-induced martensite.

6. Discussion

In some of the first investigations, Sato et al. (1986) showed that the microstructure affects the overall shape memory behaviour in these low stacking-fault energy (SFE) alloys. Defect structures harden the austenite matrix, improving the yield strength and also, a certain number of dislocations split into Schockley partial dislocations with $\frac{a}{6} < 112>_{fcc}$ Burgers vectors, forming stacking faults that act as nuclei for the ε martensite. Cast materials are soft and the dislocation density is very low. The stress needed to induce the martensitic transformation is higher than that to activated plastic deformation by perfect dislocation glide. To facilitate the γ ↔ ε (direct and reverse martensitic transformation) and improve the shape memory effect of the cast material, Otsuka et al. (1989) proposed a thermomechanical treatment called "training". After that, many authors investigated the effect of forming processes, such as rolling or forging at different temperatures, where some mechanisms of dislocation multiplication are activated. We presented the antecedents in the Introduction. Particularly, Esquivel et al. (2019) showed that adequate thermomechanical processing has the ability to optimize the SM properties, which are produced by changes introduced in the alloy's microstructure. The punch-extrusion processing that we used to manufacture seamless couplings, also affects the material. Comparing the capacities for shape recovery and the normalized torques transmitted by

the PE couplings to the couplings machined from the molten ingot (the control samples), we hypothesize that the differences could be due to the stresses developed during the reverse transformation. It seems that the microstructural changes produced by the punch-extrusion forming optimize the SME, like previously found in the rolled sheets. An analysis of microstructures by TEM is out of the scope of this work and will be presented in a forthcoming paper.

Also, the different values of maximum torque supported by the 17Mn alloy PE couplings are significant when compared to the 15Mn rolled alloy. A combination of factors affects these results. On the one hand, the 17Mn alloy exhibits retransformation stress values higher than those obtained by other Fe–Mn–Si–Cr–Ni alloys, such as Fe–15Mn–5Si–9Cr–5Ni (Druker et al., 2018) and Fe–21Mn-3.5-Si–9Cr-4.5Ni (Esquivel et al., 2019). On the other hand, the PE couplings show excellent geometric precision resulting from the internal perforation quality (optimal cylindricity). This characteristic is maintained, or even improved, after the final machining. Couplings machined directly from the cast ingot have identical geometries, but the microstructure plays a negative role, as is explained above. In contrast, the rolled and welded sheet process does not ensure cylindrical symmetry, especially in materials with a high elastic limit. The lack of cylindricity reduces the effective contact area because of poor assembly and adjustment conditions, limiting the maximum torque supported by the joint, even for materials with optimal SM properties.

We also observed that the DSR$_d$ decreases as ε_{rem} increases. Deterioration of the SME with increasing the applied strain (referred to as pre-strain in the literature) is a known effect (Li et al., 1999). At low deformations, this is almost exclusively compensated for by the γ → ε transformation, mainly through activation of the most favourably oriented crystallographic variants. At higher stress, secondary variants could be activated, accompanied by a $\sigma_{\gamma \to \varepsilon}$ transformation stress increase. This increase in stress could also be enough to activate plastic slip systems, giving rise to non-recoverable strain. Therefore, decreases in the DSR are observed. In turn, due to multiple variants and the increase in the density of martensite plates, dislocation/martensite interactions increase (Gu et al., 1994). This situation can hinder the backward movement of Shockley partial dislocations (Maji and Krishnan, 2003), impairing the material's ability for shape recovery.

Finally, we will compare the dimensional clearances afforded by the SM couplings to that of the traditional shrink-fit connection. For this later method to be used in mechanical systems, very precise tolerances are required, such that initially the inner diameter of the coupling is less than the outer diameters of the shafts and pressure alone is insufficient for assembly. In such cases, the tubular coupling is heated so that expansion reduces the level of interference making assembly possible, and then, the projected fit is achieved on cooling.

Taking into account that the shape-recovery temperature is about 400 °C, the shrinkage achieved from that temperature for a 21 mm nominal inner diameter coupling, made of plain carbon steel (α = 12 × 10^{-6}) is:

$$\Delta \varnothing = \alpha \varnothing_0 \Delta T$$

$$\Delta \varnothing = 12 x 10^{-6} \, °C^{-1} \cdot 21 \, mm \cdot 400 \, °C = 0.100 \, mm$$

which is only 0.5% of the coupling's nominal size. We found that the PE couplings which were diametrically expanded to 3% remnant deformation exhibited 75% shape recovery capacity (see section 5.2.1). Thus, the amount of deformation recovered is 2.25%, which is four times higher than that achievable with a thermal shrink coupling heated to the same temperature. If we were to heat the steel coupling to 800 °C, the shrinkage would be 1% of the nominal diameter, still much lower than the capacity of the SM coupling. Table 6 summarizes the results.

Fig. 16a shows the sliding assembly condition (considered in section 3), which ensures smooth mounting. Starting from this condition, Fig. 16b represents the SM coupling dimension after reverse
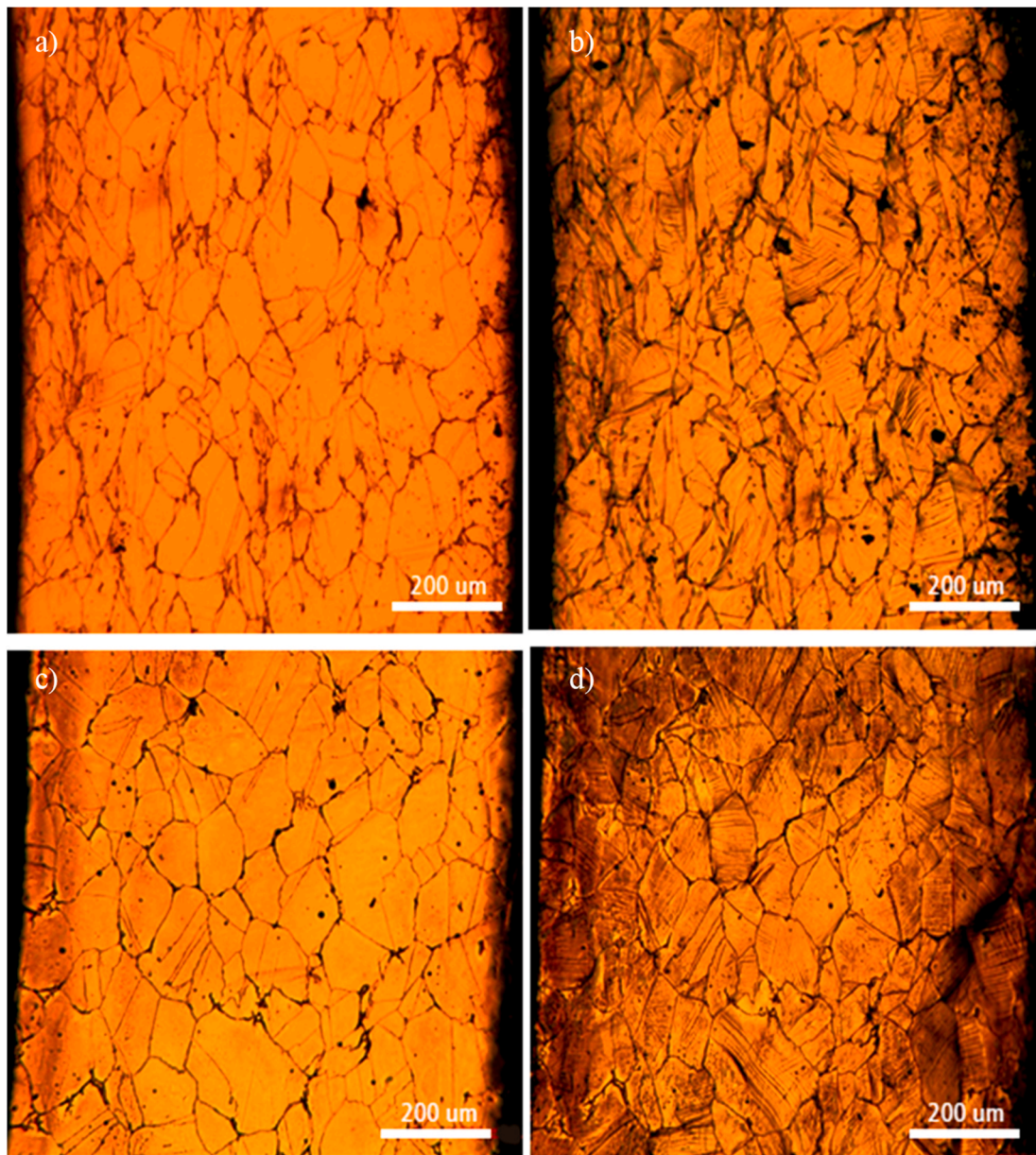
Fig. 15. Images taken from the cross sections of the PE couplings, covering the complete wall thickness. a) annealed at 700 °C before deformation, b) the same area after diametric expansion, c) annealed at 800 °C before deformation, and d) the same area after diametric expansion.

transformation (after being heated above $A_F \approx 400$ °C) and the resulting interference for this case. Contrarily, the dimensions that a steel coupling would reach by thermal shrinkage from a temperature of 800 °C are plotted in Fig. 16c, starting from the same dimensional tolerance. It can be seen that the maximum interference that would be achieved in that second case is just the same as the minimum interference in the case of the SM coupling. And, we cannot speak of minimal interference, since the most unfavourable maximum-clearance, dimensional situation will not meet the coupling objective.

The last important consideration lies in the ease of handling and the operational advantages associated with the shape memory coupling. While assembling the mechanical parts, the SM coupling is handled at room temperature in its "expanded" state, which is stable over time. In contrast, a heat shrunk joining element must be handled hot, with the difficulties that this entails, and assembly must be carried out quickly, before the coupling cools to a reduced size. The assembly period has no restrictions for SM couplings, and the parts can be assembled and disassembled as many times as desired before joining through the reverse

phase transformation at about 400 °C. The latter is very novel and is possible due to the SME.

7. Conclusions

In this work, the development and evaluation of a procedure to manufacture shape memory seamless couplings for shafts and pipes, was presented. After analysing the industrial forming methods, we adopted a fabrication system consistent with the alloy's mechanical properties and shape memory response. Thus, we designed and fabricated a prototype of a punch-extrusion die and obtained seamless tubes of satisfactory quality and length for manufacturing SM couplings. The only required finishing operation was turning to size. Finally, we measured the performance and SM properties of the PE couplings and compared them to those of couplings machined from the cast ingot. Some particular conclusions can be drawn:
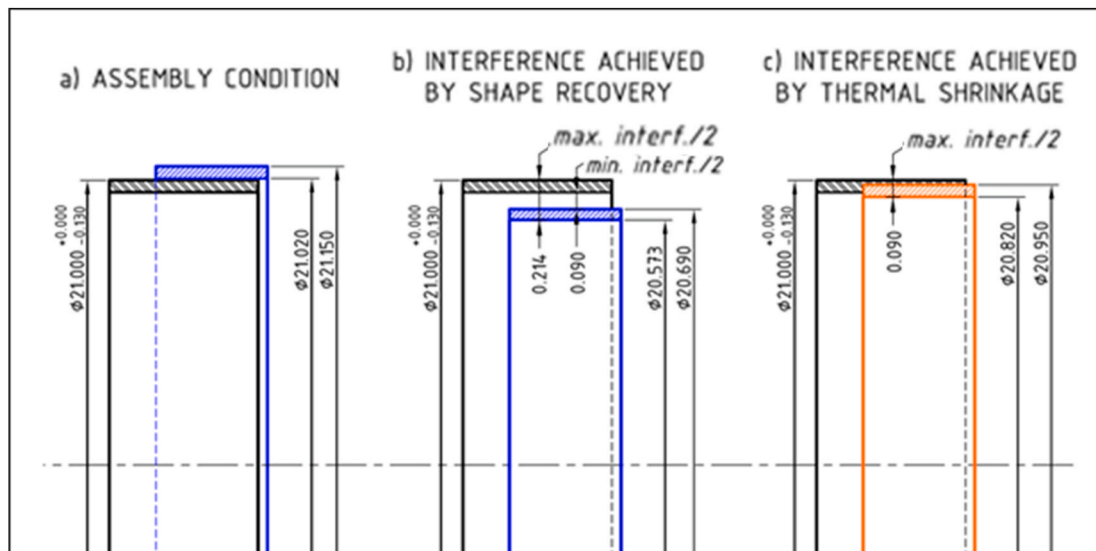
Fig. 16. Graphic representation of tolerance ranges and assembly conditions between the couplings and shafts. The dimensional range of a ⌀ 21 mm drawn shaft is shown in black, and the dimensional range of the manufactured couplings is in blue a) Slide mounting condition. b) Interference adjustment achieved by the retransformation of the SM coupling. c) Comparative example: Adjustment achieved with a shrink-fit coupling connection heated to 800 °C (the dimensions of the cold coupling are shown in orange). (For interpretation of the references to colour in this figure legend, the reader is referred to the Web version of this article.)

Table 6
Comparison between SM couplings and a steel shrink-fit connection: nominal size and shrinkage without mechanical restrictions are given.

Method	$\varnothing_{man}$ (mm)	$\varnothing_{exp}$ (mm)	$\varnothing_{ret}$(mm)	$\Delta\varnothing$(mm)	Shrinkage (%)
SM coupling	20.50	21.10	20.63	0.47	2.25
Steel shrink-fit connection					
$\Delta T = $ 400 °C	21.00	21.10	21.00	0.1	0.5
$\Delta T = $ 800 °C	20.90	21.10	20.90	0.2	1

1 The design of this particular method and the tools required for hot forming the 17Mn alloy were critical to the success of the project. We believe that this process can be extended to many other high-strength materials.

2 Separation of the process into multiple steps was an efficient solution in order to mitigate problems resulting from billet cooling during punching because it allows the alloy to be reheated. Although, a multistage process requires more time and makes the procedure more complex.

3 The PE couplings that were diametrically expanded 4% and annealed at 700 °C exhibited 75% shape recovery. In comparison, the control samples (machined from cast ingots) showed 20% less DSR_d.

4 The union of 21 mm diameter shafts by means of PE couplings annealed at 700 °C showed 40 N-m/cm^2 normalized torque transmission, which was 25% greater than that found for the cast samples. By comparing the performance of SM couplings to that of a conventional shrink-fit connection, other interesting conclusions can be drawn:

5 Interference: for the same mounting conditions – nominal size and heating to 400 °C (to ensure a complete reverse transformation of the SM coupling) – the thermal diametric contraction is 0.5% for carbon steel, while that achieved by the SM coupling is 2.25%. Moreover, if the steel's thermal contraction is activated by heating to 800 °C, the shrinkage is 1%, less than half that achieved by the SM coupling. In such a case, the maximum interference achievable by a shrink-fit connection hardly equals the minimum interference achievable by the SM couplings, and the maximum SM-coupling interference is 2.4 times higher.

6 Handling: The Fe–17Mn–6Si–10Cr–5Ni SM couplings can be handled at room temperature, while a steel thermal-contraction joint forces the coupling to be handled at high temperatures.

7 Stability: Due to natural cooling, the shrink-fit connection is unstable and must be assembled in a short time. In contrast, the designed SM couplings are stable over time, and will not undergo dimensional or microstructural changes, even up to 100–150 °C. Stability over time is a novel aspect of a shape memory coupling that allows for the final joining of the parts, by the reverse phase transformation, at a time different from that of assembly. This simplifies the assembly of complex mechanisms, for example structures that involve many parts.

Declaration of competing interest

The authors declare that they have no known competing financial interests or personal relationships that could have appeared to influence the work reported in this paper.

Acknowledgments

APPENDIX 1. EQUIPMENT

A.1. Hydraulic Press Features

The capacity and technical characteristics of the 400 kN hydraulic press used to pierce the SM alloy billet are given in Table A1. The fixed platen,

300×300 mm², is supported below by sturdy columns, while the entire power circuit, cylinder and movable platen, is supported at the top. Fig. A1 is a schematic of the original hydraulic circuit, which consists of a gear pump, a safety valve (pressure limiting), a 4-way control valve with 3 manually operated positions, and the actuator cylinder.

Table A1Technical data of the hydraulic press.

Maximum load [2]	400 kN
Cylinder stroke [1]	257 mm
Cylinder Diameter [2]	160 mm
Shank diameter [1]	138 mm
Forward (lowering) speed [1]	~12 mm/s
Reverse (climb) speed [1]	~48 mm/s
Pump	gear
Pump flow [2]	9,4 cm³/rev (14 l/min)
Motor	Three phase, 1500 rpm
Command	Manual (3-way, 2-position valve)
Pressure control	No (Only maximum pressure regulation, by safety valve)
Speed control	No
Reading items	Analog clock manometer

(1) Values measured on the equipment.
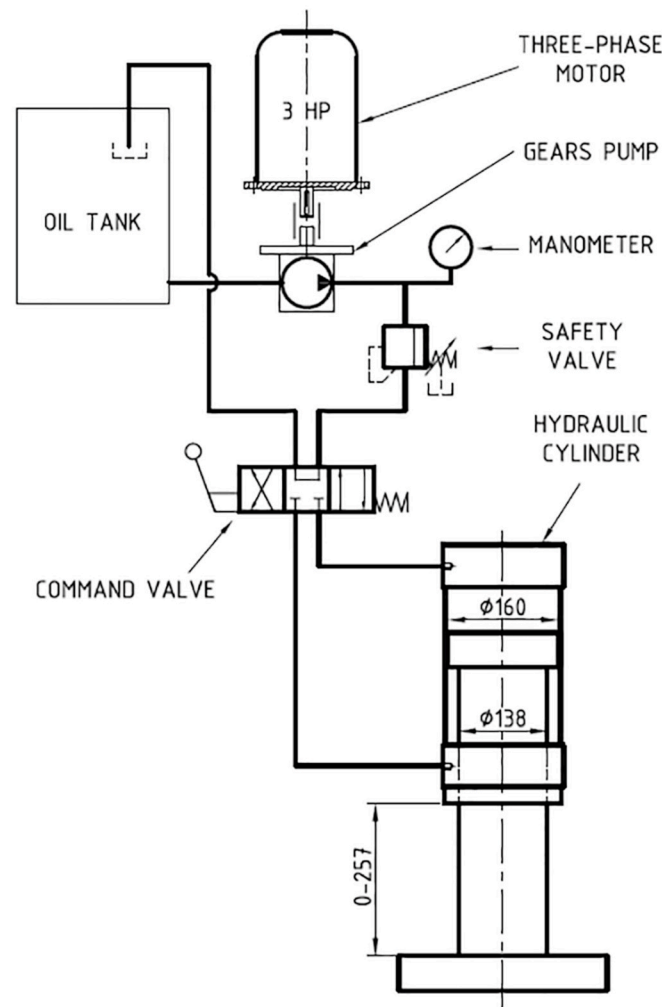(2) Values calculated based on measured values and equipment data.

Fig. A1. Details of the original hydraulic circuit.

A.2. Instrumentation and Control

The equipment was adapted to control the following:

1) Applied load

The press has only one analog pressure gauge. To obtain a digital read out of the acting pressure, an OMEGA PX119 pressure transducer and a NOVUS 1500 universal indicator with USB communication were incorporated. In order to maintain the integrity of the equipment and the tooling, we used a safety valve to limit the pressure and the maximum acting load.

2) Displacement of the punch (or the header)

To read the displacement (that is, the position of the moving header) we selected a displacement transducer OMEGA LDI-119 series with the largest displacement available, i.e. 200 mm. It is relatively inexpensive and does not need a specific power supply as it is connected to another NOVUS 1500 indicator. To avoid instrument damage, we restrict the available 257 mm hydraulic cylinder stroke to 196 mm. For this, we mount a steel collar on the piston rod to stop its travel. Both NOVUS indicators (pressure and displacement) are located in the instrument cabinet incorporated with the equipment (Fig. A2).

3) Travel speed (of the punch or header)

The working speed is determined by the flow rate from a hydraulic pump driven by a motor with a nominal rotation speed of 1500 rpm. To vary the load frame ram speed, the flow supplied to the actuator cylinder must be modified. Among the options, hydraulic, mechanical or electrical, the latter was cheaper and safer. It consists of varying the speed of the pump rotor, by means of frequency variators (drives) that supply the electric motor. We selected a SIEMENS drive, model UNIDRIVE M201. This model allows the motor to be controlled to a speed close to zero (almost down to 1 rpm). In addition, it allows enabling or disabling the motor from the command panel, or, in combination with the indicators, for certain specific values of the transducer readings.
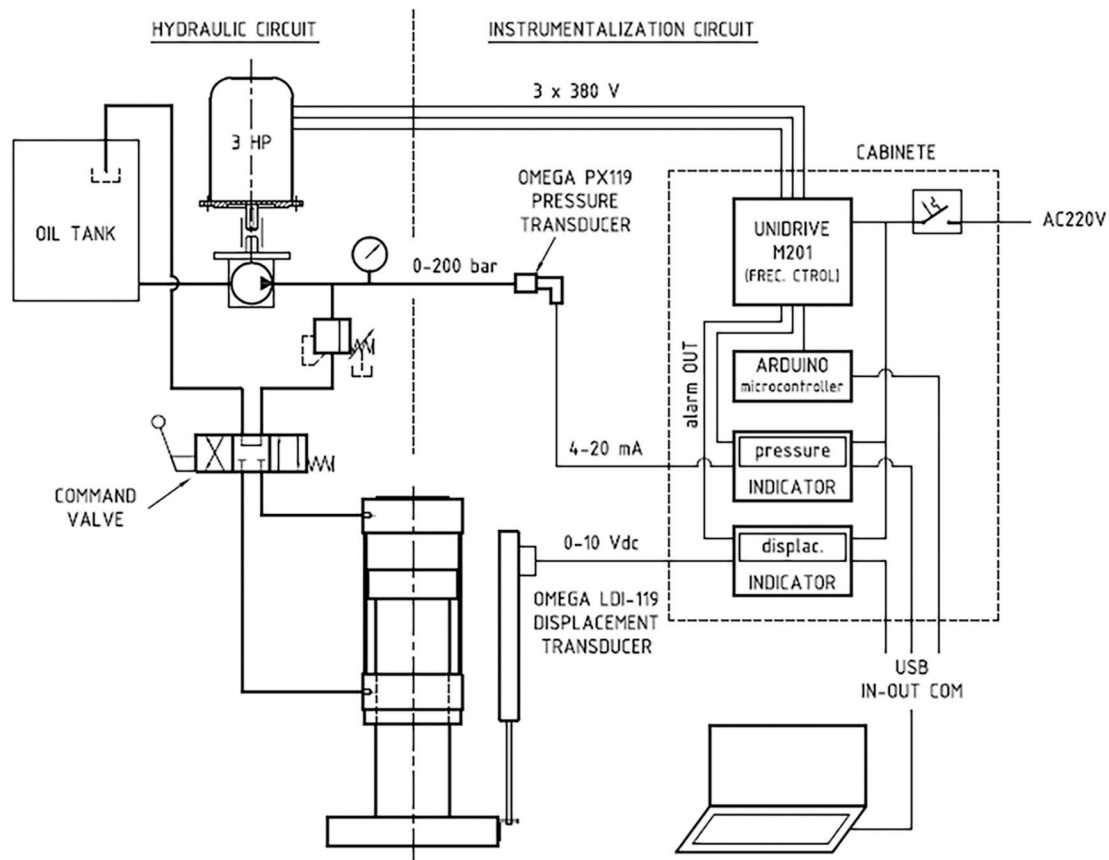

Fig. A2. Hydraulic and electric circuits, and instrumentation of the press.

APPENDIX 2. ELABORATING ON THE LOAD CALCULATIONS

The aim of this section is to find analytical expressions for the punch load, F_P, and the maximum support load, F_C. In traditional mechanical manufacturing practice (Dieter, 1961; Schuler GmbH, 1998; Groover, 2010), the working loads are calculated by equalizing the external work (W_e) with the formation work, W_d, (the work necessary to change the form of a billet with a cross-sectional area of A_0) plus the work consumed by the frictional loads, W_{fr}:

$$W_e = W_d + W_{fr} \tag{A2.1}$$

For the purpose of facilitating the calculations, we divided the working stroke into small increments of displacement, denoted as Δy. We considered

that all the loads remain constant over each increment Δy. In this way:

$$\Delta W_e = \int_{y}^{y+\Delta y} dW_e = F_e(y)\Delta y = \Delta W_d + \Delta W_{fr} \qquad \text{A2.2}$$

where, ΔW_e is the external work consumed over Δy, $F_p(y)$ is the punching load (the load externally applied) at a displacement of the punch equal to y, and ΔW_d and ΔW_{fr} are the formation work and frictional work consumed in each increment Δy, respectively.

The formation work can be expressed in terms of the change of geometric parameters (i.e., the change of the cross-sectional area of the element):

$$\Delta W_d = \sigma_f . V . \int_{y}^{y+\Delta y} d\varepsilon = \sigma_f . V . ln\frac{l_{y+\Delta y}}{l_y} = \sigma_f . V . ln\frac{A_y}{A_{y+\Delta y}} \qquad \text{A2.3}$$

where σ_f is the yield stress of the alloy at the working temperature, l_y, A_y, $l_{y+\Delta y}$, and $A_{y+\Delta y}$ are the length and cross-sectional area of the billet before and after a Δy displacement, respectively. As $\frac{A_y}{A_{y+\Delta y}}$ is the extrusion ratio $\boldsymbol{R}$ (see page 11), the formation work becomes

$$\Delta W_d = \sigma_f . V . \int_{y}^{y+\Delta y} d\varepsilon = \sigma_f . V . ln\, R \qquad \text{A2.4}$$

On the other hand, the frictional work can be express as:

$$\Delta W_{fr} = \int_{y}^{y+\Delta y} dW_{fr} = \mu . N . \Delta y = \mu . p_n . A_{contact} . \Delta y \qquad \text{A2.5}$$

where μ is the friction coefficient, at the local temperature, between the surfaces that are in-contact, and p_n is the contact pressure between the surfaces. Because it is difficult to know the precise value of μ corresponding to a particular operation, and we do not know beforehand the value of the contact pressure p_n, we approximated the product $\mu . p_n$. For this, we first consider two limits. One is the *sticking friction* case (corresponding to an absolute union between the surfaces), in which the shearing stress at the interface is equal to the shearing strength of the metal in plain strain (Dieter, 1961), thus:

$$\mu\, p_n = m\, \frac{\sigma_f}{2} \qquad \text{A2.6}$$

with $m = 1$. This criterion is usually applied in hot metalworking to set an upper bound for friction resistance. The other limit is $m = 0$, a perfect sliding condition. Accounting for these extreme cases, the factor m in *Eq. A*2.6, will describe particular frictional conditions. In our case, like in most hot working processes, frictional resistance is higher than for steel-on-steel frictional contact at room temperature (which would correspond to $m = 0.15$–0.25). But we did not observe sticking during the experimental tests. Based on these considerations, we decided to assume an average value of $m = 0.6$. Then:

$$\Delta W_{fr} = 0.6\frac{\sigma_f}{2}A_{contact} . \Delta y \qquad \text{A2.7}$$

Now, we will determine values for the loads F_P and F_C, represented in Fig. 7a and b, respectively.

a) We first consider the situation in which the punch hollows the billet, which is being held by the conical die housing (Fig. 7a). Combining equations A2.2, A2.3, and A2.7:

$$\Delta W_e = F_p(y)\Delta y = \sigma_f . V_p . ln\, R_p + 0.6\,\frac{\sigma_f}{2}\, A_{cont_{p-b}}\, \Delta y \qquad \text{A2.8}$$

where $V_p = A_0\Delta y$ is the volume deformed by the action of the punch, R_p is the reduction ratio corresponding to a displacement Δy during punching, and $A_{cont_{p-b}}$ is the contact area between the punch and the billet up to a penetration depth equal to $y + \Delta y$. Then, replacing and rearranging terms:

$$F_p(y)\, \Delta y = \sigma_f\, \Delta y\, \left(A_0\, ln\, R_p + 0.6\,\frac{1}{2}\, A_{cont_{p-b}} \right)$$

$$F_p(y) = \sigma_f\, \left(A_0\, ln\, R_p + 0.3\, A_{cont_{p-b}} \right) \qquad \text{A2.9}$$

Noting that,

$$R_p = \left[\frac{A_y}{A_{y+\Delta y}}\right]_{Punching} = \frac{\varnothing_0^2}{\varnothing_0^2 - \left(\varnothing_{p_0} + 2\,(y-4)\tan\beta\right)^2} \qquad \forall\, y > 4 \qquad \text{A2.10}$$

$$A_{cont_{p-b}} = \frac{\pi}{4}\varnothing_{p_0}^2 + \pi\,\varnothing_{p_0}\, y \qquad \text{A2.11}$$

and. $A_0 = \frac{\pi}{4}\varnothing_0^2$

We can substitute terms to obtain,

$$F_p(y) = \sigma_f \left(\frac{\pi}{4}\varnothing_0^2 \ln R_p + 0.3 \left(\frac{\pi}{4}\varnothing_{p0}^2 + \pi \varnothing_{p0} y \right) \right) \quad \forall y > 4$$

$$F_p(y) = \sigma_f \frac{\pi}{4} \left(\varnothing_0^2 \ln R_p + 0.3 \left(\varnothing_{p0}^2 + 4 \varnothing_{p0} y \right) \right) \quad \forall y > 4 \tag{A2.12}$$

b) We now consider the situation in which the action of the punch does not hollow the billet but pushes it to slide along the die (Fig. 7b). Also, the billet gets extruded due to the taper geometry of the die. Sliding is activated when the external load reaches the value of the maximum support load, that is $F_p(y) = F_s = F_C$. Then, combining equations A2.2, A2.3, and A2.7:

$$\Delta W_e = F_c \, \Delta y = \sigma_f. \, V_b . \ln R_s + 0.6 \, \frac{\sigma_f}{2} \, A_{cont_{m-b}} \, \Delta y \tag{A2.13}$$

where $V_b = A_0 l_0$ is the volume of the billet, $R_s = \frac{A_y}{A_{y+\Delta y}}$ is the reduction ratio corresponding to a displacement Δy during the sliding condition, and $A_{cont_{m-b}}$ is the contact area between the matrix and the billet. Replacing and rearranging:

$$F_c = \sigma_f \left(A_0 \, \frac{l_0}{\Delta y} \ln R_s + 0.6 \, \frac{1}{2} \, A_{cont_{m-b}} \right) \tag{A2.14}$$

where:

$$R_s = \left[\frac{A_y}{A_{y+\Delta y}} \right]_{slipping} = \frac{\varnothing_0^2}{(\varnothing_0 - 2\,\Delta y \tan \alpha)^2} \tag{A2.15}$$

$A_0 = \frac{\pi}{4}\varnothing_0^2$ and. $A_{cont_{m-b}} \approx \pi \, \varnothing_0 l_0$

It can be seen that according to this model, the critical load F_C does not depend on the punch stroke y. With respect to the value of Δy, we calculated the product $\frac{1}{\Delta y} \ln R_s$ and found that:

$$\frac{1}{\Delta y} \ln R_s \cong 0,0085 \cong constant\ with\ 0,5\ mm \leq \Delta y \leq 4\ mm$$

This means that the critical load does not depend on the specific value of Δy that appears in the calculations. Moreover, a dependence of F_C on the incremental value of Δy, lacks of physical meaning. Thus, we set $\Delta y = 1\ mm$ in order to simplify the equation. Then, replacing and rearranging terms:

$$F_c = \sigma_f \left(\frac{\pi}{4}\varnothing_0^2 \, l_0 \ln R_s + 0.6 \, \frac{1}{2} \, \pi \, \varnothing_0 l_0 \right)$$

$$F_c = \sigma_f \frac{\pi}{2} \, \varnothing_0 l_0 \left(\frac{\varnothing_0}{2} \ln R_s + 0.6 \right) \tag{A2.16}$$

where,

$$R_s = \frac{\varnothing_0^2}{(\varnothing_0 - 2 \tan \alpha)^2} \tag{A2.17}$$

References

Alves, L.M., Afonso, R.M., Silva, C.M.A., Martins, P.A.F., 2018. Joining tubes to sheets by boss forming and upsetting. J. Mater. Process. Technol. 252, 773. https://doi.org/10.1016/j.jmatprotec.2017.10.047.

Baruj, A., Troiani, H., 2008. The effect of pre-rolling Fe–Mn–Si-based shape memory alloys: mechanical properties and transmission electron microscopy examination. Math. Sci. Eng. A481, 574–577. https://doi.org/10.1016/j.msea.2007.02.140.

Comaneci, R., Zaharia, L., Nedelcu, D., Bujoreanu, L.G., 2015. Processing of cylindrical hollow parts: piercing vs. extrusion. IOP Conf. Ser. Mater. Sci. Eng. 95, 1–7. https://doi.org/10.1088/1757-899X/95/1/012032.

Dieter, G., 1961. Mechanical Metallurgy. McGraw-Hill.

Druker, A., Baruj, A., Malarría, J., 2010. Effect of rolling conditions on the structure and shape memory properties of Fe-Mn-Si alloys. Mater. Char. 61, 603–612. https://doi.org/10.1016/j.matchar.2010.03.005.

Druker, A., La Roca, P., Vermaut, P., Ochin, P., Malarría, J., 2012. Microstructure and shape memory properties of Fe–15Mn–5Si–9Cr–5Ni melt-spun ribbons. Mater. Sci. Eng., A 556, 936–945.

Druker, A., Vermaut, P., Malarría, J., 2018. The shape recovery conditions for Fe–Mn–Si alloys: an interplay between martensitic transformation and plasticity. Mater. Char. 139, 319–327.

Druker, A.V., Perotti, A., Esquivel, I., Malarría, J., 2014. A manufacturing process for shaft and pipe couplings of Fe–Mn–Si–Ni–Cr shape memory alloys. Mater. Des. 56, 878–888.

Esquivel, I., Giordana, M., Druker, A., 2019. Effect of heat treatment on the microstructure and shape memory behaviour of Fe-Mn-Si-Ni-Cr alloys. Mater. Char. 155, 109811. https://doi.org/10.1016/j.matchar.2019.109811.

Giotti, S., Fanini, S., Bruschi, S., Bariani, P.F., 2009. Modelling of the Mannesmann effect. CIRP Ann. - Manuf. Technol. 58, 255–258. https://doi.org/10.1016/j.cirp.2009.03.099.

Groover, M.P., 2010. Fundamentals of Modern Manufacturing, fourth ed. John Wiley and Sons Inc.

Gu, Q., Van Humbeeck, J., Delaey, L., 1994. A review on the martensitic transformation and shape memory effect in Fe-Mn-Si alloys. J. Phys. IV, 135–144. https://doi.org/10.1051/jp4:1994319.

Hu, C., Yin, Q., Zhao, Z., 2017. A novel method for determining friction in cold forging of complex parts using a steady combined forward and backward extrusion test. J. Mater. Process. Technol. 249, 57–66. https://doi.org/10.1016/j.jmatprotec.2017.06.001.

Kajikawa, S., Kuboki, T., Iizuka, T., 2021. Flange compression using stepped punch for forming extremely deep cup with flange from aluminum alloy sheet. J. Mater. Process. Technol. 288, 116835. https://doi.org/10.1016/j.jmatprotec.2020.116835.

Kajiwara, S., 1999. Characteristic features of shape memory effect and related transformation behavior in Fe-based alloys. Mater. Sci. Eng. 275, 67–88. https://doi.org/10.1016/S0921-5093(99)00290-7.

Kajiwara, S., Liu, D., Kikuchi, T., Shinya, N., 2001. Remarkable improvement of shape memory effect in Fe-Mn-Si based shape memory alloys by producing NbC precipitates. Scripta Mater. 44, 2809–2814. https://doi.org/10.1016/S1359-6462(01)00978-2.

Kumar, U., Kumar Mishra, A., Ohdar, R., 2014. Hot forging lubricants. Int. Jour. of Mech. Eng. and Rob. Res. 3, 155–162.

Lee, Y., Choi, C., 2000. Driving force for γ↔ε martensitic transformation and stacking fault energy of γ in Fe-Mn binary system. Metall. Mater. Trans. 31A, 355. https://doi.org/10.1007/s11661-000-0271-3.

Li, H., Dunne, D., Kennon, N., 1999. Factors influencing shape memory effect and phase transformation behaviour of Fe–Mn–Si based shape memory alloys. Mater. Sci. Eng. A273–275, 517–523. https://doi.org/10.1016/S0921-5093(99)00391-3.

Li, J.C., Zhao, M., Jiang, Q., 2000. Alloy design of FeMnSiCrNi shape-memory alloys related to stacking-fault energy. Metall. Mater. Trans. 31A, 581. https://doi.org/10.1007/s11661-000-0001-x.

Maji, B., Krishnan, M., 2003. The effect of microstructure on the shape recovery of a Fe–Mn–Si–Cr–Ni stainless steel shape memory alloy. Scripta Mater. 48, 71–78. https://doi.org/10.1016/S1359-6462(02)00348-2.

Marré, M., Gies, S., Maevus, F., Tekkaya, A.E., 2010. Joining of lightweight frame structures by die-less hydroforming. Int. J. Material Form. 3 (Suppl. 1), 1031.

Nishiyama, Z., Fine, M.E., Meshii, M., Wayman, C.M., 1978. Martensitic Transformation. Academic Press, New York).

Oberg, E., Jones, F.D., Horton, H.L., Ryffel, H.H., 2004. "Machinery's Handbook", 27th Edition. Industrial Press Inc.

Otsuka, H., Murakami, M., Matsuda, S., 1989. Proceed. Of the M.R.S. Int. Meeting on Advanced Materials 9. Shape Memory Materials, Tokyo, Japan, p. 451.

Otsuka, K., Wayman, C.M., 1998. Shape Memory Materials. Cambridge University Press, New York.

Peng, H., Wang, G., Wang, S., Chen, J., MacLaren, I., Wen, Y., 2018. Key criterion for achieving giant recovery strains in polycrystalline Fe-Mn-Si based shape memory alloys. Mater. Sci. Eng. A712, 37–49. https://doi.org/10.1016/j.msea.2017.11.071.

Sato, A., Chishima, E., Soma, K., Mori, T., 1982. Shape Memory effect in γ ↔ ε transformation in Fe-30Mn-1Si alloy single crystals. Acta Metall. 30, 1177. https://doi.org/10.1016/0001-6160(82)90011-6.

Sato, A., Yamaji, Y., Mori, T., 1986. Physical properties controlling shape memory effect in Fe-Mn-Si alloys. Acta Metall. 34, 287.

Sawaguchi, T., Maruyama, T., Otsuka, H., Kushibe, A., Inuoe, Y., Tsuzaki, K., 2016. Design concept and applications of Fe-Mn-Si-Based alloys –from shape-memory to seismic response control. Mater. Trans. 57 (3), 283–293. https://doi.org/10.2320/matertrans.MB201510.

Schuler GmbH, 1998. Metal Forming Handbook. Springer.

Sivasankaran, S., Ramkumar, K.R., Ammar, H., Al-Mufadi, F., Alaboodi, A., Irfan, O., 2021. Microstructural evolutions and enhanced mechanical performance of novel Al-Zn die-casting alloys processed by squeezing and hot extrusion. J. Mater. Process. Technol. 292, 117063. https://doi.org/10.1016/j.jmatprotec.2021.117063.

Stanford, N., Dunne, D., 2006. Thermo-mechanical processing and the shape memory effect in an Fe–Mn–Si-based shape memory alloy. Mater. Sci. Eng. A422, 352–359. https://doi.org/10.1016/j.msea.2006.02.009.

Tsuzaki, K., Natsume, Y., Kurokawa, Y., Maki, T., 1992. Improvement of the shape memory effect in Fe-Mn-Si alloys by the addition of carbon. Scripta Metall. Mater. 27, 471–473. https://doi.org/10.1016/0956-716X(92)90213-X.

Weber, F., Gebhard, J., Gitschel, R., Goyal, S., Kamaliev, M., Wernicke, S., Tekkaya, A.E., 2021. Joining by forming – a selective review. J. Adv. Join. Proces. 3, 100054. https://doi.org/10.1016/j.jajp.2021.100054.

Wen, Y.H., Peng, H.B., Raabe, D., Gutierrez-Urrutia, I., Chen, J., Du, Y.Y., 2014. Large recovery strain in Fe-Mn-Si-based shape memory steels obtained by engineering annealing twin boundaries. Nat. Commun. 5, 4964. https://doi.org/10.1038/ncomms5964.

Wick, C., Benedict, J., Veilleux, R. (Eds.), 1984, TME Handbook, fourth ed., II. FORMING, Society of Manufacturing Engineers.

Zhoua, W., Yu, J., Lin, J., Dean, T., 2020. Effects of die land length and geometry on curvature and effective strain of profiles produced by a novel sideways extrusion process. J. Mater. Process. Technol. 282, 116682. https://doi.org/10.1016/j.jmatprotec.2020.116682.